



**Stratocumulus Cloud Clearings: Statistics from Satellites, Reanalysis Models, and Airborne Measurements**

Hossein Dadashazar<sup>1</sup>, Ewan Crosbie<sup>2,3</sup>, Mohammad S. Majdi<sup>4</sup>, Milad Panahi<sup>5</sup>, Mohammad A. Moghaddam<sup>5</sup>, Ali Behrangi<sup>5</sup>, Michael Brunke<sup>5</sup>, Xubin Zeng<sup>5</sup>, Haflidi H. Jonsson<sup>6</sup>, Armin Sorooshian<sup>1,5\*</sup>

<sup>1</sup>Department of Chemical and Environmental Engineering, University of Arizona, Tucson, AZ, USA

<sup>2</sup>Science Systems and Applications, Inc., Hampton, VA, USA

<sup>3</sup>NASA Langley Research Center, Hampton, VA, USA

<sup>4</sup>Department of Electrical and Computer Engineering, University of Arizona, Tucson, AZ, USA

<sup>5</sup>Department of Hydrology and Atmospheric Sciences, University of Arizona, Tucson, AZ, USA

<sup>6</sup>Naval Postgraduate School, Monterey, CA, USA

\*Corresponding author: armin@email.arizona.edu



18 Abstract

19 This study provides a detailed characterization of stratocumulus clearings off the U.S. West  
20 Coast using remote sensing, reanalysis, and airborne in situ data. Ten years (2009-2018) of  
21 Geostationary Operational Environmental Satellite (GOES) imagery data are used to quantify the  
22 monthly frequency, growth rate of total area ( $GR_{Area}$ ), and dimensional characteristics of 306 total  
23 clearings. While there is interannual variability, the summer (winter) months experienced the most  
24 (least) clearing events with the lowest cloud fractions being along coastal topographical features  
25 along the central to northern coast of California including especially just south of Cape Mendocino  
26 and Cape Blanco. From 09:00 to 18:00 (PST), the median length, width, and area of clearings  
27 increased from 680 to 1231 km, 193 to 443 km, and  $\sim 67,000$  to  $\sim 250,000$  km<sup>2</sup>, respectively.  
28 Machine learning was applied to identify the most influential factors governing the  $GR_{Area}$  of  
29 clearings between 09:00-12:00 PST, which is the time frame of most rapid clearing expansion.  
30 The results from Gradient Boosted Regression Tree (GBRT) modeling revealed that air  
31 temperature at 850 hPa ( $T_{850}$ ), specific humidity at 950 hPa ( $q_{950}$ ), sea surface temperature (SST),  
32 and meridional wind speed at 850 hPa ( $V_{850}$ ) were most impactful in enhancing  $GR_{Area}$ . Clearings  
33 have distinguishing features such as an enhanced Pacific high shifted more towards northern  
34 California, offshore air that is warm and dry, stronger coastal surface winds, enhanced lower  
35 tropospheric static stability, and increased subsidence. Although clearings are associated obviously  
36 with reduced cloud fraction where they reside, the domain-averaged cloud albedo was actually  
37 slightly higher on clearing days as compared to non-clearing days. To validate speculated  
38 processes linking environmental parameters to clearing growth rates based on satellite and  
39 reanalysis data, airborne data from three case flights were examined. Measurements were  
40 compared on both sides of the clear-cloudy border of clearings at multiple altitudes in the boundary  
41 layer and free troposphere, with results helping to support links suggested by model simulations.  
42 More specifically, airborne data revealed extensive horizontal shear at cloud-relevant altitudes that  
43 promoted mixing between clear and cloudy air. Vertical profile data provide support for warm and  
44 dry air in the free troposphere additionally promoting expansion of clearings. Airborne data  
45 revealed greater evidence of sea salt in clouds on clearing days, pointing to a possible role for, or  
46 simply the presence of, this aerosol type in clearing areas coincident with stronger coastal winds.

47  
48



## 49 1. Introduction

50 Stratocumulus clouds play an important role in both global and regional climate systems.  
 51 Stratocumulus clouds are the dominant cloud type over marine environments based on annual  
 52 mean of area covered (Warren et al., 1986; Hahn and Warren, 2007). In coastal areas, these clouds  
 53 can impact industries such as agriculture, transportation (e.g., aviation), military operations,  
 54 coastal ecology, and biogeochemical cycles of nutrients. Stratocumulus clouds also play an  
 55 important role in the global radiation budget due to their high albedo contrast with the underlying  
 56 ocean surface. Challenges in accurately simulating the presence and properties of stratocumulus  
 57 clouds include the difficulty in separating the influence of microphysical and dynamical factors  
 58 and the existence of multiple feedbacks in cloud systems (Brunke et al., 2019). Therefore, accurate  
 59 characterization of cloud formation and evolution is critical.

60 Numerous studies have examined the behavior of clouds off the United States (U.S.) West  
 61 Coast (e.g., Coakley et al., 2000; Durkee et al., 2000; Stevens et al., 2003; Lu et al. 2009; Painemal  
 62 and Minnis, 2012; Modini et al., 2015; Sanchez et al., 2016). The persistence of the cloud deck in  
 63 this region, especially during the summer, makes it a key location for studying marine  
 64 stratocumulus clouds. Furthermore, the prevalence of freshly-emitted aerosols from ships provides  
 65 an optimal setting for field measurements of aerosol-cloud-precipitation interactions because of  
 66 the relative ease of finding strong aerosol perturbations, from which cloud responses can be  
 67 robustly quantified (e.g., Russell et al., 2013). Over the decades of research conducted in the  
 68 aforementioned study region and two other major stratocumulus regions (Southeast Pacific Ocean  
 69 off the Chile-Peru coasts and Southeast Atlantic Ocean off the Namibia-Angola coasts), one  
 70 feature that has not received sufficient attention is large scale stratocumulus clearings that are  
 71 easily observed in satellite imagery and often exceed 100 km in width (Fig. 1). Perhaps the most  
 72 obvious impact of these clearings is the change in albedo as an otherwise cloudy area would be  
 73 highly reflective. Improving understanding of factors governing clearings has implications for  
 74 modeling of marine boundary layer clouds and for operational forecasting of weather and fog along  
 75 coastlines.

76 Previous studies have documented the existence of large scale cloud clearings off the U.S.  
 77 West Coast (e.g., Kloesel, 1992). During the 2013 Nucleation in Cloud Experiment (NiCE), three  
 78 case study flights with the Center for Interdisciplinary Remotely-Piloted Aircraft Studies  
 79 (CIRPAS) Twin Otter examined clearings off the California coast, with a focus on diurnal behavior  
 80 and contrasting aerosol and thermodynamic properties across the cloud-clearing interface (Crosbie  
 81 et al., 2016). Based on a multi-day event, they showed that a clearing expanded during the day and  
 82 contracted at night towards the coast with oscillations between growth and decay over the multi-  
 83 day clearing lifetime. They observed that small scale processes (~1 km) at the clearing-cloud  
 84 border are influential in edge dynamics that likely upscale to more climatologically influential  
 85 scales, which is why reanalysis data cannot accurately replicate the spatial profile of cloud fraction  
 86 and cloud liquid water path when compared to satellite data. One of their three events was  
 87 associated with a so-called “southerly surge”, also referred to as a coastally-trapped disturbance  
 88 (CTD). CTD events were recently characterized off the U.S. West Coast by Juliano et al. (2019a,b).  
 89 Clearing events have been examined over the southeast Atlantic Ocean with the catalyst for cloud  
 90 erosion shown to be atmospheric gravity waves (Yuter et al., 2018). While these aforementioned  
 91 studies have explained details associated with clearings in different coastal regions, there are many  
 92 unanswered questions remaining and a need for more statistics associated with clearings to build  
 93 more robust conclusions.



The goal of this work is to build upon cloud clearing studies over the U.S. West Coast to provide a more comprehensive analysis using the synergy of data from satellite remote sensors, reanalysis products, and airborne in-situ measurements. We first examine a decade of satellite data to report on statistics associated with the temporal and spatial characteristics of clearings. These characteristics are then studied in conjunction with environmental properties from reanalysis products and machine learning simulations to identify factors potentially contributing to the formation and evolution of clearings. Lastly, airborne in situ data are used to validate findings from the aforementioned analyses and to gain more detailed insight into specific events that otherwise would not be possible with reanalysis and satellite products. The most significant implications of our results are linked to modeling of fog and boundary layer clouds, with major implications for a range of societal and environmental issues such as climate, military operations, transportation, and coastal ecology.

## 2. Experimental Methods

### 2.1 Satellite Datasets

Long-term statistics associated with clearings were obtained using Geostationary Operational Environmental Satellite (GOES) visible band ( $\sim 0.6 \mu\text{m}$ ) images. Visual imagery data were obtained from GOES-11 for 2009 through 2011 and from GOES-15 between 2012 and 2018 (data products summarized in Table 1). Images were analyzed for the spatial domain bounded by  $115^\circ$ - $135^\circ$  W and  $30^\circ$ - $50^\circ$  N. The following steps led to the identification of individual clearings using GOES images, of which a total of 306 were identified between 2009 and 2018:

- (i) GOES-11 and GOES-15 visible images were obtained from the National Oceanic and Atmospheric Administration (NOAA) Comprehensive Large Array-data Stewardship System (CLASS) database (<http://www.class.noaa.gov>).
- (ii) Each day's sequence of GOES images were visually inspected to identify if a clearing event was present.
- (iii) For each clearing event, four images were selected to both quantify clearing properties and characterize diurnal variability: (i) Image 1 after sunrise, between 14:15 UTC (7:15 Pacific Standard Time (PST)) and 16:45 UTC (09:45 PST) with a median at  $\sim 16:00$  UTC (09:00 PST); (ii) Image 2 at a time relevant to the Moderate Resolution Imaging Spectroradiometer (MODIS) Terra overpass over the study region, between 18:45 UTC (11:45 PST) and 20:45 UTC (13:45 PST) with a median at  $\sim 19:00$  UTC ( $\sim 12:00$  PST); (iii) Image 3 at a time relevant to the MODIS Aqua overpass over the study region, ranging from 19:45 UTC (12:45 PST) to 22:15 UTC (15:15 PST) with a median at  $\sim 22:00$  UTC ( $\sim 15:00$  PST); and (iv) Image 4 before sunset, ranging from 22:45 UTC (15:45 PST) to 02:15 UTC (19:15 PST) with a median at  $\sim 01:00$  UTC ( $\sim 18:00$  PST). For the purposes of subsequent discussion, local times (PST) will be used.
- (iv) A custom-made cloud mask algorithm was applied consisting of the following steps: (i) each visible image was converted to an 8-bit integer gray-scale image with values assigned to each pixel ranging from 0 (black) to 255 (white); (ii) continental areas were masked from the analysis (i.e., green regions in Fig. 1), meaning that their values were not included in subsequent steps; (iii) a histogram of values for all pixels over the ocean was calculated for each image obtained in the previous step and then Otsu's method (Otsu 1979) was applied on the obtained histogram to compute a global threshold to categorize each pixel



as either clear or cloudy; (iv) a MATLAB image processing toolbox was used to extract the clearing as an object, including the pixels at the clearing-cloud border and pixels inside the clearing; (v) information contained within the clear pixels was then used to estimate clearing dimensions such as width, length, area, and centroid for the spatial domain bordered by 115°-135° W and 30°-50° N; and (vi) a MATLAB application was written to automate all of the aforementioned steps to process data for a decade (2009-2018).

Data were used from the MODIS on the Terra and Aqua satellites to characterize cloud and aerosol properties on clearing and non-clearing days in the spatial domain of analysis defined above. Daily Level 3 Collection 6.1 data (Hubanks et al., 2019) with spatial resolution 1°×1° were downloaded from the LAADS DAAC distribution system (<https://ladsweb.modaps.eosdis.nasa.gov/>). The key daytime parameters (Table 1) retrieved for this study relevant to liquid clouds included the following: cloud fraction (CF) obtained from the MODIS cloud mask algorithm (Platnick et al., 2003), cloud optical thickness ( $\tau$ ), cloud liquid water path (LWP), and cloud droplet effective radius ( $r_e$ ). Detailed information about these MODIS products is described elsewhere (Platnick et al., 2003; Platnick et al., 2017; Hubanks et al., 2019).

Although MODIS Level 3 data parameters do not include cloud droplet number concentration ( $N_d$ ), previous studies estimated  $N_d$  using retrievals of  $\tau$  and  $r_e$  with assumptions (Bennartz, 2007; Painemal and Zuidema, 2010; McCoy et al., 2017). We use the following equation from Painemal and Zuidema (2010) to estimate  $N_d$ :

$$N_d = \frac{(\Gamma_{ad})^{\frac{1}{2}}}{k} \frac{10^{\frac{1}{2}}}{4\pi\rho_w^{\frac{1}{2}}} \frac{\tau^{\frac{1}{2}}}{r_e^{\frac{5}{2}}} \quad (1)$$

where  $\rho_w$  is the density of liquid water,  $\Gamma_{ad}$  is the adiabatic lapse rate of liquid water content (LWC), and the parameter  $k$  is representative of droplet spectral shape as the cube of the ratio between the volume mean radius and the effective radius. While Painemal and Zuidema (2010) used a  $\Gamma_{ad}$  value equal to  $2.0 \times 10^{-4} \text{ g m}^{-4}$  to estimate  $N_d$  for the southeast Pacific region, we use the average value of  $\Gamma_{ad} = 2.3 \times 10^{-4} \text{ g m}^{-4}$  reported by Braun et al. (2018) for the northeast Pacific. A constant value of 0.8 (Martin et al. 1994) is assigned to  $k$  in Equation 1.

Similar to our previous study on clearings (Crosbie et al., 2016), cloud top albedo ( $A$ ) was quantified using  $\tau$  in the following relationship (Lacis and Hansen 1974):

$$A = \frac{\tau}{\tau + 7.7} \quad (2)$$

## 2.2 Reanalysis Data

Various products from Modern-Era Retrospective analysis for Research and Applications, Version 2 (MERRA-2; Gelaro et al., 2017) were used to gain insight into possible mechanisms influencing the formation and evolution of clearings off the U.S. West Coast. MERRA-2 data were downloaded from the NASA Goddard Earth Sciences Data and Information Services Center (GES DISC; <https://disc.gsfc.nasa.gov/>). Table 1 summarizes MERRA-2 parameters used in this work, including detailed information such as their product identifier and temporal resolution.



## 181 2.3 Airborne In-Situ Data

182 Motivated by the three case study research flights (RFs) probing clearings during the NiCE  
 183 campaign (Crosbie et al., 2016), the Fog and Stratocumulus Evolution Experiment (FASE) was  
 184 carried out with nearly the same payload on the Center for Interdisciplinary Remotely-Piloted  
 185 Aircraft Studies (CIRPAS) Twin Otter between July and August 2016 (Sorooshian et al., 2018).  
 186 Data were used from three case RFs examining clearings: RF08 on 2 August 2016, and  
 187 RF09A/RF09B on 3 August 2016. The back-to-back flights on 3 August afforded an opportunity  
 188 to examine the evolution of clearing properties at the clear-cloudy interface over a span of a few  
 189 hours. Figure 2 shows GOES imagery and the flight pattern for RF09A, which is representative of  
 190 the other two shown in Figs. S1–S2. The same flight strategy from NiCE (Crosbie et al., 2016) was  
 191 used in the FASE RFs and included the following set of maneuvers (Fig. 2c): (i) spiral profiles on  
 192 both sides of the clear-cloudy interface; (ii) level legs extending on both sides of the clear-cloudy  
 193 interface near the ocean surface (~30 m; called “surface leg”), above cloud base, and mid-cloud;  
 194 (iii) a series of sawtooth maneuvers up and down between ~60 m below and above the cloud top  
 195 on both sides of the clear-cloudy interface; and a (iv) level leg in the free troposphere (FT) at ~1  
 196 km altitude.

197 Commonly used instruments provided dynamic, thermodynamic, and navigational data  
 198 (Crosbie et al., 2016; Dadashazar et al., 2017; Sorooshian et al., 2018). Of the relevance to this  
 199 study are 10 Hz measurements of wind speeds, air temperature, and humidity. Setra pressure  
 200 transducers attached to a five-hole gust probe radome provided three components of wind speeds  
 201 after correction for aircraft motion, which was obtained by a C-MIGITS-III GPS/INS system.  
 202 Ambient air temperature was measured by a Rosemount Model 102 total temperature sensor. Also,  
 203 humidity data were collected with an EdgeTech Vigilant chilled mirror hygrometer (EdgeTech  
 204 Instruments, Inc.).

205 Cloud micro/macrophysical parameters were measured at 1 Hz with various instruments.  
 206 Size distributions of cloud droplets and rain droplets were characterized using the Forward  
 207 Scattering Spectrometer Probe (FSSP;  $D_p \sim 2\text{--}45 \mu\text{m}$ ) and Cloud Imaging Probe (CIP;  $D_p \sim 25\text{--}$   
 208  $1600 \mu\text{m}$ ). LWC data were obtained using a PVM-100 (Gerber et al., 1994), which were vertically  
 209 integrated during sounding profiles to quantify cloud LWP. Aerosol concentration data are  
 210 reported here from the passive cavity aerosol spectrometer probe (PCASP;  $D_p \sim 0.11\text{--}3.4 \mu\text{m}$ ;  
 211 Particle Measuring Systems (PMS), Inc.; modified by Droplet Measurement Technologies, Inc.)  
 212 at 1 Hz time resolution. Cloud water composition data were obtained using a modified Mohnen  
 213 slotted-rod collector (Hegg & Hobbs, 1986) that was manually placed out of the aircraft during  
 214 cloud passes to collect cloud water. The collected samples were analyzed for water-soluble ions  
 215 using ion chromatography (IC; Thermo Scientific Dionex ICS-2100 system) and water-soluble  
 216 elements using triple quadrupole inductively coupled plasma mass spectrometry (ICP-QQQ;  
 217 Agilent 8800 Series). Liquid-phase concentrations of species were converted to air-equivalent  
 218 units ( $\mu\text{g m}^{-3}$ ) via multiplication with the sample-averaged LWC. The reader is referred to other  
 219 works for more extensive discussion about cloud water collection and sample analysis from FASE  
 220 and other recent CIRPAS Twin Otter campaigns (Crosbie et al., 2018; Prabhakar et al., 2014;  
 221 Sorooshian et al., 2013a; Wang et al., 2016; Youn et al., 2015).

222 Ten Hz measurements of environmental parameters were used to estimate turbulent  
 223 variance and covariance flux values. To perform the aforementioned calculations, collected data  
 224 for wind speed and temperature were de-trended using a 2-km wide high pass filter that utilizes a  
 225 minimum order-filter with a stopband attenuation of 60 dB and transition band steepness of 0.95.  
 226 Friction velocity ( $u^*$ ) was calculated from the surface leg following the method provided in Stull





(1988) and Wood (2005). In addition, convective velocity ( $w^*$ ) was estimated by implementing the buoyancy integral method (Nicholls and Leighton, 1986). Turbulent kinetic energy (TKE) in the marine boundary layer (MBL) is generated by two main mechanisms, specifically shear and buoyancy generation. Following Wood (2005), the ratio of the MBL depth ( $z_i$ ) to the Monin–Obukhov length ( $L_{MO}$ ) was estimated as a way to determine the relative influence of shear versus buoyancy in values of TKE. Large positive values of the ratio ( $-z_i/L_{MO}$ ) are associated with the turbulence in the MBL governed more with buoyancy production, while small or negative values are associated with the dominance of shear production.

Properties relevant to the inversion layer were estimated from sawtooth maneuvers above and below the cloud top, which typically coincided with the inversion base altitude (Fig. 2c). The inversion base height was defined as the altitude where the ambient temperature first reached its minimum above the sea surface (Crosbie et al., 2016). Inversion top was defined as the highest altitude with the gradient in liquid water potential temperature over altitude in the inversion layer ( $d\theta_l/dz$ ) exceeding  $0.1 \text{ K m}^{-1}$ .  $d\theta_l/dz$  was calculated from linear fits over a moving window of 75 points from 10 Hz data. The following characteristics were estimated and reported for the inversion layer: (i) inversion base height; (ii) inversion top height; (iii) inversion depth; (iv) jump in liquid water temperature ( $\Delta\theta_l$ ); (v) maximum gradient of the potential temperature ( $(d\theta_l/dz)_{\max}$ ); (vi) drop in the total moisture ( $\Delta q_t$ ); and (vii) change in the horizontal wind speed ( $\Delta U$ ).

## 2.4 Clearing Growth Modeling Using Machine Learning

A Gradient Boosted Regression Tree (GBRT) model approach was implemented to investigate the impact of environmental parameters on the evolution of clearing events. GBRT models have been successfully used in past work to study low-level clouds (Fuchs et al., 2018). The Scikit-Learn library (Pedregosa et al., 2011) was used for careful parameter tuning in order to accurately represent the data and desired relationships without overfitting the model (Fuchs et al., 2018).

We apply the GBRT model to analyze clearing growth rates of total area ( $GR_{\text{Area}}$ ) obtained from the comparative analysis between GOES Image 1 (~9:00 PST) and Image 2 (~12:00 PST) or each of the 306 events. As will be shown, the most rapid clearing growth occurs between 9:00 and 12:00 PST among the three time increments between Images 1–4 (i.e., 09:00 – 18:00 PST). Here we describe how the predictor values were obtained. A rectangular box was placed around the larger of the clearing areas from Image 1 or 2 for each clearing event using the maximum and minimum values of both latitude and longitude. The same size rectangular box was then placed on the other image using identical latitude and longitude bounds. MERRA-2 data were then obtained for each  $0.5^\circ \times 0.625^\circ$  grid within the rectangular area for the two images, and then averaged for the pair of images. Each grid was also assigned the value of the clearing  $GR_{\text{Area}}$  for the entire clearing (i.e., each grid had the same value of  $GR_{\text{Area}}$  assigned to it). Parameters used in the modeling included those relevant to aerosol (aerosol optical depth (AOD)), thermodynamics (air temperature (T), air specific humidity (q), and sea-surface temperature (SST)), and dynamic variables (mean sea level pressure anomaly ( $MSLP_{\text{anom}}$ ), zonal wind speed (U), meridional wind speed (V), planetary boundary layer height (PBLH), and vertical pressure velocity ( $\omega$ )). Most of the aforementioned variables were first analyzed at different vertical levels including the surface, 950 hPa, 850 hPa, and 700 hPa in order to then filter variables out to keep only the most appropriate input parameters.

Model simulation results are reported in terms of a parameter termed ‘partial dependence’ (PD) following methods in earlier works (e.g., Friedman, 2001; Fuchs et al., 2018). PD plots



represent the change of the clearing  $GR_{Area}$  relative to a selected parameter by marginalizing over the remaining predictors. For each given value of a selected parameter ( $x_s$ ), partial dependence ( $PD(x_s)$ ) can be obtained by computing the average of model outputs using the training data as shown in Equation 3:

$$PD(x_s) = \frac{1}{n} \sum_{i=1}^n \hat{f}(x_s, x_R^{(i)}) \quad (3)$$

where  $\hat{f}$  is the machine learning model,  $x_R$  are the remaining parameters, and  $n$  is the number of instances in the training data. PD profiles were computed between the 1st and 99th percentile of each selected parameter.

To correctly interpret the model output using the PD criterion and gradient boosting, it was required that the model input parameters not be correlated. Thus, the input parameters were chosen so as to have the least correlation among them. Two input parameters were determined to be independent if a linear regression between the two parameters yielded an  $r^2$  value of less than 0.5. For instance, there were three choices of air temperature (i.e., at 950, 850, and 700 hPa), but based on the  $r^2$  criterion, only one ( $T_{850}$ ) was used in the model, as it proved to be an independent input parameter. Lower tropospheric stability (LTS: defined as the difference between the potential temperature of the free troposphere (700 hPa) and the surface) is the stability parameter that has been widely used as a key factor controlling the coverage of stratocumulus clouds. However, in this study, the effects of stability were examined by putting  $T_{850}$  and SST into the model without explicitly including LTS. The correlation between LTS and  $T_{850}$  prevented them to be used as input parameters simultaneously. Using  $T_{850}$  and SST instead of LTS is advantageous because the results can be more informative by revealing different impacts of the two individual parameters on the model's output rather than just one parameter in the form of LTS. In addition, the mean sea level pressure anomaly ( $MSLP_{anom}$ ) was used as an input parameter, which was calculated in reference to the average values of MSLP for the summer months for the study period. In the end, the following eleven predicting variables from MERRA-2 were used as input parameters for the GBRT simulations, with data product details summarized in Table 1: AOD,  $T_{850}$ ,  $q_{950}$ ,  $q_{850}$ ,  $q_{700}$ , SST,  $MSLP_{anom}$ ,  $U_{850}$ ,  $V_{850}$ , PBLH, and  $\omega_{700}$ .

To train, test, and validate the statistical models, the dataset was split into random parts. The training set was comprised of 75% of the data points, 30% of which were randomly selected for validation. This process helped reduce variance and increase model robustness. The remaining 25% of the data points comprised the test dataset. The model setup was tuned using training data, for which different scenarios were tested that were specified by a parameter grid through a 10-fold cross-validated search. The model was run on the dataset 30 times to achieve robust results. To qualitatively rank the input parameters based on their influence on growth rates, differences between the maximum and minimum of PD ( $\Delta PD$ ) were calculated over 30 runs.

### 3. Results and Discussion

#### 3.1 Temporal and Spatial Profile of Clearings

##### 3.1.1 Monthly and Interannual Trends

The frequency of clearing events was quantified for the three summer months (June – July – August, JJA) of each year between 2009 and 2018 (Fig. 3). Note that if a clearing event lasted multiple days as in the case of the 11-day clearing probed by Crosbie et al. (2016), it was counted separately for each individual day rather than assigned a value of one for a multi-day period. There was considerable interannual variability, with clearing events ranging between a minimum of 14 in 2017 and a maximum of 45 in 2011. The relative percentage of total days in the summer season





having clearings ranged from 15.2% – 48.9% with a mean  $\pm$  standard deviation of  $33.3 \pm 10.9$  days. The specific month with the most clearing events varied between years, with August typically having the least number of events among the summer months. The most recent year of the decade examined, 2018, was used to more closely examine the distribution of clearing events as a function of all 12 months. Daily probabilities of clearing events are shown for each month, with the highest probability between May and September ( $> 0.2$ ), especially June ( $\sim 0.42$ ). Daily probabilities were lowest in the winter season, with January having no clearings (0).

To identify if the monthly profile of clearings is biased by the monthly profile of CF, Figs. S3-S4 show the mean annual cycle of MODIS CF for 2018 and 2009-2018, respectively. The range in CFs for 2018 and 2009-2018 were 0.59-0.76 and 0.60-0.74, respectively, with the mean values being  $0.69 \pm 0.05$  and  $0.68 \pm 0.04$ . This is indicative of relatively low variability. A reasonable question is if August had the lowest clearing daily probability of the summer months because it potentially had the lowest CF. Figs. S3-S4 do not show significant variations in CF between the summer months, with mean values in 2018 for June, July, and August being 0.71, 0.72, and 0.72, respectively. Also, the lowest mean daily probability in 2018 was for January and February, but those months do not exhibit the lowest CF (January = 0.76, February = 0.67). Rather, September exhibited the lowest CF (0.59). Finally, CF decreased from 0.72 to 0.59 from August to September 2018, but the daily probability of clearings actually increased slightly. Thus, the systematic changes in CF between months are not the primary cause for inter-monthly variation in clearing formation.

### 3.1.2 Diurnal

Dimensional characteristics of cloud clearings as a function of time of day are summarized here. The median width of clearings was smallest in the morning at 09:00 (193 km), with an increase between 09:00 and 12:00, and then a leveling off in expansion until 18:00 (443 km) (Fig. 4). Clearing length and area followed the same qualitative trend in growth with an initial increase and then leveling off. The median length and area of clearings at 09:00 were 680 km and  $\sim 67,000$  km<sup>2</sup>, respectively, with values at 18:00 being  $\sim 1231$  km and  $\sim 250,000$  km<sup>2</sup>. The aspect ratio (width:length) was of interest to quantify how long such clearings are relative to their width throughout the day, with results indicating a minor increase that was more linear than asymptotic (from  $\sim 0.32$  at 09:00 to  $\sim 0.37$  at 18:00). Although the range in median values was very small, there was significant variability at each of the four time steps shown. Figure 5 quantifies the GR of total area, width, and length by comparing 12:00 to 09:00, 15:00 to 12:00, and 18:00 to 15:00. The GRs for clearing length, width, and area are expectedly lowest from 15:00 to 18:00 and highest from 09:00 to 12:00.

Figure 6 shows cloud fraction maps for the times corresponding to panels 1 – 4 for all 306 events between 2009 and 2018. The spatial maps show that the centroid of the clearings is generally focused on the coastal topographical features along the central to northern coast of California including especially just south of Cape Mendocino and Cape Blanco. The 09:00 map most clearly shows that those two topographical features potentially serve as ‘trigger points’ for the majority of clearings, and as a typical clearing day develops, the cloud fraction gets reduced around those points by moving farther south and to the west. Juliano et al. (2019a/b) also discussed the significance of these capes in their analysis of CTDs pointing to their ability to alter local dynamics, cloud depth, and various microphysical processes such as entrainment. Southerly wind during CTDs promotes cloud thinning on the northern side of the capes due to an expansion fan effect (Juliano et al., 2017).



### 3.2 Contrasting Clearing and Non-Clearing Cases

Large-scale characteristics of a dynamic and thermodynamic nature (parameters in Table 1) were contrasted between clearing and non-clearing days (Fig. 7). Sub-daily data were averaged up to daily resolution for parameters of interest, which were subsequently used to produce a climatology for non-clearing (614 days) and clearing (306 days) cases for the summers between 2009 and 2018. We further calculated the difference between clearing and non-clearing conditions.

The Pacific high usually sets up a few hundred kms west of California during the summertime, which promotes northerly flow near the surface along the coastline (e.g., Juliano et al., 2019a). As compared to non-clearing cases, clearing days are characterized by having an enhanced Pacific high shifted more towards northern California (Fig. 7). In both cases (clearing and non-clearing), the cross-coast gradient in MSLP and 850 hPa geopotential height gradients are the highest in northern California and directed away from the coast. Due to the displacement of the Pacific high towards the northeast part of the study region on clearing days, these gradients are much more profound on clearing days as compared to non-clearing days. This results in a  $2\text{--}5\text{ m s}^{-1}$  increase in northerly surface wind speed (Fig. 8a) between  $35^{\circ}\text{N}$  and  $45^{\circ}\text{N}$ . Looking at the 850 hPa wind field (Fig. 8b), there is also a  $\sim 2\text{--}5\text{ m s}^{-1}$  increase in wind speed but in this case more in a northeasterly direction, which equates to having offshore flow from the northern California coast. The tightening of the 850 hPa geopotential height gradient on clearing days results in strong offshore flows by Cape Blanco and Cape Mendocino (Fig. 8a) where cloud fraction minima are observed (Fig. 6). Average conditions at 500 hPa indicate mostly westerly flow on both clearing and non-clearing days. Non-clearing days exhibited a weak trough offshore, while during clearing days a ridge is present at 500 hPa farther offshore, which can be attributed to the stronger high-pressure system on clearing days.

The difference in air temperature between clearing and non-clearing cases at the surface reaches up to  $\sim 0.7\text{ K}$  on the western edge of the study domain (Fig. 7a). Clearing cases exhibited cooler temperatures closer to the coast where the clearings develop and evolve. SST shows a similar pattern as air temperature at the surface (Fig. 9a). Faster offshore winds at the surface can promote ocean upwelling and thus cooler SSTs, as was also observed for CTD events in the same region (Juliano et al., 2019a). Furthermore, the generally high cloud fractions during clearing days for the entire spatial domain reduces radiative transfer to the ocean, also acting to reduce SST over the broader study region. It is well-documented that cloudiness and surface winds play a major role in influencing SSTs (e.g., Klein et al., 1995). In contrast, air temperatures at higher levels (850 and 500 hPa) are enhanced adjacent to the coastline in clearing cases. Air temperature at 850 hPa is higher (lower) to the south (north) of Cape Blanco and Cape Mendocino (Fig. 6) in clearing cases as compared to non-clearing cases, with the difference reaching as high as  $\sim 2\text{ K}$ . The enhanced offshore flow of warm and dry air in the vicinity of Cape Blanco and Cape Mendocino likely contribute to why many of the clearings geographically are centered at these coastal topographical features (Fig. 6).

Concomitant with higher cloud fraction and reduced SSTs, the study region also exhibited generally higher LTS by up to  $\sim 2\text{ K}$  on clearing days versus non-clearing days (Fig. 9b). Other works have pointed to the connection between cooler SSTs, higher boundary layer cloud amount, and increased stability in the lower atmosphere (Norris and Leovy 1994, Klein and Hartman 1993). With enhanced LTS values on clearing days, it is expected that there will be simultaneously strong subsidence. This is indeed confirmed in Fig. 9c using  $\omega_{700}$  as the proxy variable, with the strongest difference between clearing and non-clearing days (up to  $\sim 0.1\text{ Pa s}^{-1}$ ) off the coast Cape Blanco



and Cape Mendocino and geographical coincident with where the sharpest gradients occur for MSLP between clearing and non-clearing cases (Fig. 7). It is interesting to note that the maximum values in LTS coincide spatially with  $\omega_{700}$  on non-clearing days, in contrast to clearing days when the peak value of  $\omega_{700}$  is farther north from where LTS peaks.

Another key environmental parameter related to MBL cloud coverage is the PBLH. Regardless of whether clearings were present, PBLH generally increases with distance from the coast (Fig. 9d), similar to SST. PBLH tends to be higher on clearing days though, with the largest differences observed to the north off the coasts of Washington and British Columbia. The smallest differences existed where the majority of clearings evolved, specifically off the California coast. The maps of cloud fraction from MODIS Terra (Fig. 10a) can provide at least one possible explanation for the spatial differences in PBLH between clearing and non-clearing days. Cloud fraction is generally higher for the broad study region on clearing days, which leads to more opportunity for cloud top radiative cooling to then fuel turbulence in MBL. Greater turbulence can lead to a deeper MBL. But in the one area where PBLHs are not enhanced for the clearing days, off the California coast, cloud fractions are reduced, which is why PBLH does not exhibit greater values and actually has lower PBLH values.

Figure 9e shows spatial maps of specific humidity at 10 m above the sea surface ( $q_{10m}$ ), which serves as a proxy of available moisture in MBL. Assuming a shallow and well-mixed MBL,  $q_{10m}$  represents moisture levels in that MBL. Similar to SST,  $q_{10m}$  increases to the south of the study region with especially reduced values immediately adjacent to the California coast. Comparing clearing and non-clearing days, the former is less humid in the MBL (up to  $-0.6 \text{ g kg}^{-1}$ ). This is at least partly attributed to offshore flow and entrainment of dry continental air. Specific humidity was also examined at 850 hPa, which is closer to the vertical layer more relevant to air impacting cloud top close to the coastline. Figure 9f shows that  $q_{850}$  was substantially lower (up to  $\sim -1.2 \text{ g kg}^{-1}$ ) in the clearing cases, especially in the regions where most of the clearings occur. Drier air above cloud top will decrease cloudiness through entrainment processes. It is interesting to note that the area of greatest  $q_{850}$  difference (Fig. 9f) corresponds to the area of greatest northeasterly winds in the difference plot of the wind field at 850 hPa (Fig. 8b). These pieces of evidence point to the role of dry continental air in contributing to the formation and sustenance of clearings via offshore flow.

Another important parameter influencing MBL clouds is nuclei of the cloud droplets, specifically the cloud condensation nuclei (CCN). CCN in the region originate from a blend of sources, including natural ones (sea spray, marine and continental biogenic emissions, terrestrial dust), biomass burning, ship exhaust, and continental anthropogenic sources (Hegg et al., 2010; Coggon et al., 2014; Wang et al., 2014; Maudlin et al., 2015; Mardi et al., 2018). As a representation of the general level of aerosol pollution in the region, spatial maps are shown for Aerosol Optical Depth (AOD), which is a columnar measurement of aerosol extinction (Fig. 9g). In general, regions closer to the shore exhibit higher values of AOD on non-clearing days, with especially higher levels north of  $40^\circ \text{ N}$ . It is unclear as to why this is, since stronger winds on clearing days along the coast have the potential for more emissions from marine biogenic sources (via upwelling), sea spray, and offshore continental flow. Although based on speculation, one of many possible explanations could be that stronger fluxes of sea spray on clearing days have the potential to expedite the drizzle formation process in polluted clouds via broadening of cloud droplet size distributions, which leads to wet scavenging of aerosols in the study region (Dadashazar et al., 2017; Jung et al., 2015; MacDonald et al., 2018; Sorooshian et al., 2013b).



South of Cape Blanco and Cape Mendocino on clearing days, there were pockets of high AOD relative to other coastal locations, which is presumed to be linked to stronger winds and offshore continental flow; this is analogous to how CTD events exhibit more pollution north of these coastal features when there is southerly flow (Juliano et al., 2019a). That the greatest AOD differences occur close to the coast warrant additional research as they may be suggestive of variations in ocean-land-atmosphere interactions that result from the movement and strengthening of the Pacific high during clearing events. Future work should examine if such AOD differences on clearing versus non-clearing days are linked to differences in MBL sources and sinks (i.e., wet scavenging), or FT processes.

Spatial maps of cloud microphysical variables provide consensus that clearing days generally have higher  $N_d$  and reduced values of  $r_e$ ,  $\tau$ , and LWP near the California coast where clearings form and evolve (Fig. 10). Figure S5 shows the same qualitative results based on MODIS Aqua data for cloud microphysical parameters. Lower LWP values on clearing days near the coast are consistent with offshore flow of dry and warm air eroding clouds. The combination of higher  $N_d$  and lower LWP by the coastline results in smaller  $r_e$  on clearing days. The more polluted clouds along the coastline during clearing days, especially south of major capes, is analogous to CTD clouds being more polluted during southerly wind regimes in the study region (Juliano et al., 2019a/b). An intriguing aspect of clearing days was that although a significant section of the study region was cloud-free, the mean cloud albedo ( $A$ ) over the entire study domain was actually slightly higher than on non-clearing days (Fig. 10f). More specifically, the domain-averaged  $A$  values based on MODIS Terra data (and using Eq. 2) were 0.50 and 0.53 for non-clearing and clearing cases, respectively. The corresponding values using MODIS Aqua data were 0.48 and 0.50, respectively.

### 3.3 Modeling of Clearing Growth Rates

It has been already shown (Figs. 4-6) that clearings exhibit diurnal variability in dimensional characteristics, with rapid growth between 09:00 and 12:00 PST. It is of interest now to examine what environmental parameters control the growth within this 3 h period based on the 306 clearing cases between 2009 and 2018. The GBRT modeling method was used to this end based on the method described in Section 2.4.

The coefficient of determination ( $r^2$ ) between predicted and observed clearing growth rates for the 30 randomly selected testing datasets ranged between 0.52 to 0.77 with an average of 0.65. A multivariate linear regression model using the LASSO method (Tibshirani, 1996) was also applied to the obtained dataset to assess the performance of the GBRT model in comparison to the linear model. The  $r^2$  value of the linear model varied between 0.08 and 0.11 with an average of 0.10, revealing the poor performance as compared to the GBRT model. As noted in at least one previous study (Klein 1997), linear models can explain less than 20% of the variance in low cloud amount on daily time scales. This is in contrast to monthly time scales for which such models perform much better and can explain over 50% of the variance (Klein and Hartmann, 1993; Norris and Leovy, 1994). Part of the success of the GBRT model to model clearing growth rates can be attributed to the complexity of the model, specifically its ability to capture non-linearity between clearing growth rates and environmental parameters.

As there is independence between model parameters, the range of PDs for each individual environmental parameter is used here as a proxy for the sensitivity of clearing growth rates to that specific parameter. Higher PD ranges translate to a higher sensitivity of  $GR_{Area}$  to that specific parameter, indicating that it is a major influential factor. The range of partial dependence (PD) of



clearing growth rates for all the parameters included in the GBRT model is provided in Fig. 11, moving from left to right in order of highest to lowest PD ranges. Figure 12 shows the profiles of PD for  $GR_{Area}$  ( $PD_{GR_{Area}}$ ) relative to each individual parameter tested, where increasing values of  $PD_{GR_{Area}}$  indicate that the corresponding change on the x-axis for the value of the specific parameter is conducive to faster clearing growth.

Figure 11 displays the PD of clearing  $GR_{Area}$  for the range of change in environmental parameters used in the GBRT model. The top-ranking parameter with the highest PD range was air temperature at 850 hPa ( $T_{850}$ ). The difference in PD range from  $T_{850}$  to the next best parameter ( $q_{950}$ ) was the greatest between any other consecutive pair of parameters.  $T_{850}$  is closely linked to inversion strength variables such as LTS (Klein and Hartmann, 1993) and estimated inversion strength (EIS) (Wood and Bretherton, 2006). At constant SST, higher  $T_{850}$  translates to higher EIS and LTS values. It is well-established that inversion strength plays a key role in controlling MBL cloud coverage (Klein and Hartmann, 1993). It is expected that higher  $T_{850}$  decreases (increases)  $GR_{Area}$  (cloud amount) by enhancing stability. Figure 12a shows that up to 290 K, the profile of PD exhibits a downward trend as  $T_{850}$  increases. Above 290 K, PD of  $GR_{Area}$  starts to show the opposite trend with increasing  $T_{850}$ . As noted in Brueck et al. 2015, "...increased stability is a necessary but not a controlling factor for cloudiness, especially not when it is already sufficiently large. A further increase in inversion strength may thus further limit cloudiness, because it increases the entrainment of relatively drier and warmer air...". Figure 7b showed that  $T_{850}$  was enhanced off the California coast on clearing days, pointing to the high potential for warm continental air to impact the underlying cloud deck via entrainment. It is important to note that, when the model was run with the same set of parameters but replacing  $T_{850}$  with LTS, the PD profile of LTS exhibited a qualitatively similar trend to what was presented for  $T_{850}$  in Fig. 12a.

The moisture content at 950 hPa was the second most influential parameter. The  $PD_{GR_{Area}}$  profile of  $q_{950}$  shows increasing values as  $q_{950}$  decreases below  $8 \text{ g kg}^{-1}$ , coincident with dry air that can dissipate clouds and aid in clearing formation and expansion. Further, the  $PD_{GR_{Area}}$  of  $q_{850}$  showed a sharp decrease below values of  $2 \text{ g kg}^{-1}$ , whereas  $PD_{GR_{Area}}$  leveled off above  $2 \text{ g kg}^{-1}$ . In contrast to the other level heights, the  $PD_{GR_{Area}}$  profile of  $q_{700}$  exhibits an opposite trend but a smaller influence on  $GR_{Area}$  (Fig. 12j). This can be partly due to the fact that this layer of the FT is not as close to the cloud layer, which in turn can permit other factors besides the entrainment process to stand out. These various humidity parameters clearly show that conditions of dry air close to the MBL top help clearings form and expand, with the most likely source being continental air. The positive relationship between humidity at the level of clouds and low-level cloud amount was reported in earlier studies (Albrecht 1981; Bretherton et al., 1995; Wang et al., 1993).

Sea surface temperature and  $V_{850}$  were the next most influential parameters. As previously explained, lower SST values are associated with cloudiness and increased LTS (Norris and Leovy 1994, Klein and Hartman 1993). Figure 12d displays the dependence of  $PD_{GR_{Area}}$  on  $V_{850}$ , which is representative of flow in the FT. As discussed already, clearings coincided with strong northerly flow at 850 hPa, which is consistent with the sharp increase in  $PD_{GR_{Area}}$  as northerly wind speeds increased above  $10 \text{ m s}^{-1}$  while otherwise being flat for lower speeds. Stronger northerly flow is associated with offshore flow of dry and warm air that can reside above the cloud top, which can dissipate the cloud layer after entrainment and via enhanced shearing (via Kelvin-Helmholtz instability) and mixing of cloudy parcels with warm and dry air in the FT. As will be shown later,





544 aircraft data showed that typical wind speeds parallel to clear-cloudy interfaces were near or  
 545 greater than  $10 \text{ m s}^{-1}$  (Fig. 13).

546 Several parameters followed  $V_{850}$  in ranking with  $PD_{\text{GRArea}}$  ranges similar to one another:  
 547 PBLH,  $q_{850}$ ,  $MSLP_{\text{anom}}$ , and  $U_{850}$ . For PBLH, Figure 12e suggests that above  $\sim 600 \text{ m}$ ,  $PD_{\text{GRArea}}$  is  
 548 relatively insensitive to positive perturbations in PBLH, but below  $\sim 600 \text{ m}$ , the shallower the  
 549 MBL, the lower the value of  $PD_{\text{GRArea}}$ . This potentially can be attributed to the fact that a shallower  
 550 MBL could be more well-mixed and moisture can get transported from the ocean surface to the  
 551 cloud layer which promotes cloudiness (Albrecht et al., 1995). Figure 12g shows that for  $MSLP_{\text{anom}}$   
 552 between  $\sim -560 \text{ Pa}$  and  $\sim 450 \text{ Pa}$ , perturbations do not have much impact on  $GR_{\text{Area}}$ . However,  
 553 above  $\sim 450 \text{ Pa}$ ,  $GR_{\text{Area}}$  is more susceptible to positive perturbations in MSLP. This confirms that  
 554 stronger Pacific high conditions in the study region promote the expansion of clearing events  
 555 during the day. Also,  $GR_{\text{Area}}$  is highly sensitive to MSLP anomalies below  $\sim -560$ ; this can be  
 556 attributed to a decrease in the dominant pressure system in the region, which is not the optimal  
 557 condition to sustain the cloud layer. Based on the  $PD_{\text{GRArea}}$  profiles in Fig. 12h, clearings expanded  
 558 faster as  $U_{850}$  increased above  $0 \text{ m s}^{-1}$  and decreased below  $-3 \text{ m s}^{-1}$ .

559 There was low variability in the range of  $PD_{\text{GR}}$  for the rest of the parameters shown in Fig.  
 560 11: AOD,  $q_{700}$ , and  $\omega_{700}$ . Figure 12i shows a decrease in  $PD_{\text{GRArea}}$  as AOD increases up to the value  
 561 of  $\sim 0.12$ , above which  $PD_{\text{GRArea}}$  increases as a function of AOD. While it is expected that stronger  
 562 northerly winds associated with clearing expansion promote higher sea salt fluxes (i.e., higher  
 563 AOD), future work is warranted to investigate as to whether this process subsequently depletes  
 564 cloud water and thins out clouds via expedited drizzle production via broadening of cloud droplet  
 565 size distributions, as already suggested in Section 3.2.

566 The relationship between  $\omega$  at  $700 \text{ hPa}$  and  $PD_{\text{GRArea}}$  is complex. Brueck et al. (2015)  
 567 suggested that enhanced  $\omega_{700}$  promotes cloudiness due to its link to higher LTS. Myers and Norris  
 568 (2013) further showed that stronger subsidence can reduce cloud fraction (at fixed inversion  
 569 strength) by pushing down the top of the MBL, which is also supported by Bretherton et al. (2013).  
 570 The  $PD_{\text{GRArea}}$  profile of  $\omega_{700}$  exhibited a minimum point near a value of  $0 - 0.2 \text{ Pa s}^{-1}$ , with increases  
 571 in  $GR_{\text{Area}}$  below and above that range. The increase in  $PD_{\text{GRArea}}$  with higher  $\omega$  values above  $0.2 \text{ Pa}$   
 572  $\text{s}^{-1}$  can be attributed to the negative influence of subsidence on lower cloud fraction (via pushing  
 573 down the top of the MBL) as discussed by Myers and Norris (2013). Conversely, the increase in  
 574  $GR_{\text{Area}}$  with decreasing  $\omega$  values below  $0 \text{ Pa s}^{-1}$  can be due to upward motion reducing the strength  
 575 of the inversion capping the MBL, which is important to sustain the cloud deck.

576 It is important to caution that the interpretation of results from the GBRT simulations are  
 577 speculative and rooted in documented physical relationships between the various parameters  
 578 shown in Figs. 11-12 and low cloud behavior. One way to try to validate some of the conclusions  
 579 above is with airborne data for case studies. For instance, in situ data can help confirm the nature  
 580 of factors discussed above during clearing events, including vertically-resolved winds, primary  
 581 marine aerosol fluxes in different wind regimes, humidity and temperature of air within and  
 582 above the MBL, and potential for mixing of air above and below the MBL top. The next section  
 583 is an attempt to conduct this exercise using three airborne case studies.

584  
 585





### 586 3.4 Airborne Case Studies

587 To gain a more detailed perspective on clearings in the study region, three case flights are  
 588 examined from the 2016 FASE airborne campaign. For context, Crosbie et al. (2016) examined  
 589 three different case flights during the 2013 NiCE campaign and provided the following insights,  
 590 which motivated the FASE flights for further statistics: (i) two of the three clearings (RF19 on 1  
 591 August 2013, RF23 on 7 August 2013) were immediately adjacent to the coastline and had reduced  
 592 humidity in the MBL on the clearing side, suggestive of dry continental offshore wind laterally  
 593 mixing into and dissipating clouds; (ii) the latter two cases also had enhanced temperature in the  
 594 clear column at cloud-relevant altitudes, which help explain the lack of clouds in the clear column;  
 595 (iii) the other clearing flight (RF16 on 29 July 2013) had the clearing positioned to the west of a  
 596 cloud deck, which was associated with a CTD event along the coastline to the east of the clearing  
 597 (i.e., southerly surge). This case exhibited warmer temperatures in the clear column only in the top  
 598 100 m of the MBL with similar humidity profiles, but with cooler and moister air above the  
 599 inversion base in the clear column. This case was suspected to be linked to entrainment and mixing  
 600 of dry air into the cloud deck to produce the clearing, but it was not a case of  
 601 subsidence/divergence, otherwise the air in the clear column would have been warmer and drier  
 602 above the inversion base.

603 For the three FASE case flights, the clearing was always situated to the west of a cloud  
 604 deck touching the coastline (Figs. 2, S1-S2). This positioning is reminiscent of NiCE RF16, which  
 605 was less sensitive to lateral entrainment of continental air in comparison to the other two NiCE  
 606 flights. Wind data were decomposed into  $u$  and  $v$  components to represent speeds that are  
 607 perpendicular and parallel, respectively, to the clear-cloudy interface. Figure 2d illustrates an  
 608 example of how these two components of winds varied during RF09A. There were substantial  
 609 changes in  $v$  on the two sides of the clear-cloud border, with stronger northerly winds on the clear  
 610 side, reaching as high as  $20 \text{ m s}^{-1}$ , in contrast to about half that magnitude on the cloudy side. The  
 611 same substantial change in  $v$  across the interface was also present in RF08 and RF09B with  
 612 stronger  $v$  winds always on the clear side. There was no substantial change in the  $u$  component of  
 613 wind speed between the two columns in each of the three flights.

614 To extend upon the possibility of shearing effects, absolute changes in  $v$  ( $|v|$ ) were  
 615 calculated for level legs performed at the clear-cloudy border for the three research flights (Table  
 616 2). For consistency, these calculations were based on level legs of a constant length of  $\sim 40 \text{ km}$   
 617 with relatively equal spacing on both sides of the clear-cloudy border.  $|v|$  was calculated by  
 618 multiplying  $40 \text{ km}$  by the slope of the linear fit of  $v$  versus distance from cloud edge, where  
 619 negative (positive)  $x$  values represent distance away from the edge on the clear (cloud) side. The  
 620 results reveal that the horizontal wind shear was strongest somewhere between mid-cloud and  
 621 cloud top altitudes, with the lowest values at the FT level. The lowest values in the MBL were  
 622 observed in the surface legs. Shear at the clear-cloudy edge, especially at cloud levels, can support  
 623 clearing growth through enhancing the mixing of cloudy and clear air. Crosbie et al. (2016) also  
 624 showed using the case of NiCE RF19 that that mixing of cloudy air with adjacent clear air can be  
 625 an important contributor to cloud erosion and thus expansion of clearings. To probe deeper into  
 626 the clearing cases, the subsequent discussion compares vertically-resolved data on both sides of  
 627 the clear-cloudy border based on soundings and level legs.

#### 628 3.4.1 RF08

629 RF08 (2 August 2016) represented a case similar to the NiCE RF16 (29 July 2013) case  
 630 study in Crosbie et al. (2016) where cooler and moister air above the inversion in the clear column  
 631



was speculated to be due to entrainment and mixing eroding the cloud rather than subsidence and divergence catalyzing cloud dissipation. Of note is that there was rapid infill of cloud the night of the NiCE FR16 flight. FASE RF08 data showed that potential temperature was warmer ( $\sim 1$  K) in the MBL of the clear column as compared to the cloudy column, while in the FT, the air was slightly warmer on the cloudy side (Fig. 13). SST was also approximately 0.4 K higher in the clear column (Table 3). Specific humidity was almost identical in the MBL on both sides, but air was moister above the inversion base on the clear side. As noted above, vertical profiles of  $u$  revealed little difference between the two columns, but  $v$  values were nearly twice as high in the clear column extending from the surface to approximately 200 m above cloud top. Surface wind speeds were also enhanced on the clear side, which resulted in greater friction velocity ( $u^* = 0.40 \text{ m s}^{-1}$  vs  $0.15 \text{ m s}^{-1}$  on the cloudy side).

An important feature was the wind maximum in and above the inversion layer on the clear side, which resulted in larger vertical shear across the inversion on the clear side ( $5.44 \text{ m s}^{-1}$ ) compared with the cloudy side ( $0.8 \text{ m s}^{-1}$ ) (see  $\Delta U$ , Table 3). The strong shear on the clear side likely facilitated mixing of MBL air with drier and warmer FT air. This is supported by a lower temperature gradient  $(\Delta\theta/\Delta z)_{\text{max}}$  in the inversion layer of the clear column ( $0.32 \text{ K m}^{-1}$  vs  $0.38 \text{ K m}^{-1}$ ), which was thicker than the cloudy column (82 m vs 55 m). A further effect of the wind maximum in the clearing was to increase moisture advection, counteracting the accumulation of moisture caused by mixing induced by vertical shear. This was most significant at the cloud top level as seen in the largest difference in the edge-parallel wind  $|v|$  (Table 2). In the absence of cloud, the effects of longwave radiative cooling close to the cloud top level would be subdued allowing shear-induced mixing to erode the sharpness of the inversion. Redistribution of moisture into the inversion also serves to insulate lower layers from longwave cooling, further delaying the formation of cloud. The difference in  $|v|$  was smallest close to the surface, indicating that the wind maximum in the clearing had a (comparatively) lesser effect in enhancing surface moisture fluxes. Satellite imagery confirms that later in the day, the cloud layer filled-in partially where the clearing was with the presumed help of nocturnal radiative forcing.

The cloud layer in RF08 was the thinnest (131 m) with the shallowest MBL among all three cases. In addition, the lowest  $N_d$  ( $107 \text{ cm}^{-3}$ ), largest  $r_e$  ( $6.6 \mu\text{m}$ ), and highest cloud base rain rate ( $0.48 \text{ mm day}^{-1}$ ) was measured in RF08 of all three cases. The enhanced rain can likely explain why the surface aerosol concentrations from the PCASP were lowest in RF08 ( $106\text{--}108 \text{ cm}^{-3}$  vs  $186\text{--}236 \text{ cm}^{-3}$  for the other two flights) even though surface winds were highest, specifically due to efficient wet scavenging of aerosols. This possibility is at least linked to the speculation reported earlier in Sections 3.2 and 3.3 that stronger northerly winds linked to the growth of clearings result in sea salt expediting rain formation in clouds and thus thinning them out. In support of this notion, cloud water composition results are of relevance as they provide an indication of the relative influence of giant CCN (GCCN) in the form of sea salt, as previously demonstrated in the region by Dadashazar et al. (2017). The combined concentration of sodium ( $\text{Na}^+$ ) and chloride ( $\text{Cl}^-$ ) was  $60 \mu\text{g m}^{-3}$ ,  $33 \mu\text{g m}^{-3}$ , and  $64 \mu\text{g m}^{-3}$  for RF08, RF09A, and RF09B, respectively. In contrast, the average combined sum of  $\text{Na}^+$  and  $\text{Cl}^-$  for all samples collected in FASE was  $14 \mu\text{g m}^{-3}$ . Based on a two-tailed student's  $t$ -test with 95% confidence, the means of RF08 and RF09B were significantly different than the mean of all FASE samples. The  $\text{Cl}^-:\text{Na}^+$  mass ratios in all three FASE clearing flights (RF08 = 1.80, RF09A = 1.78, RF09B = 1.79) were very close or matching that of pure sea salt (1.81), providing more confidence that sea salt was impacting these clouds via serving as CCN. The cloud water results are in support of GCCN enhancing drizzle in RF08 and thus thinning out clouds and removing aerosol underneath the cloud base. It is unclear with this



dataset though as to what role the impact of sea salt in depleting clouds of their water had to do with the actual clearing, but at least there is support for this process potentially impacting the cloudy column. Consistent with the NiCE clearing cases, aerosol concentrations were relatively similar on both sides of the clear-cloudy border for all three FASE cases.

Figure 14 displays turbulence parameters such as variance in the three components of wind speed (Fig. 14a-c) and buoyancy flux (Fig. 14d). Stronger horizontal wind speeds, and consequently stronger shear production, near the surface on the clear side resulted in greater variance in the horizontal wind components at all MBL levels. Both  $\overline{u^2}$  and  $\overline{v^2}$  exhibit a general downward trend with increasing altitude, which is also supportive of shear driven turbulence. On the other hand,  $\overline{w^2}$ , which is closely associated with cloud layer properties, exhibits a different trend on the cloudy side as it increases from base to mid-cloud level. For surface and above cloud base levels,  $\overline{w^2}$  is higher in the clear column likely due to the combined influence of shear and buoyancy terms on the turbulence budget. On the other hand, in the mid-cloud layer,  $\overline{w^2}$  is slightly higher (Fig. 14c) in the cloudy column as compared to clear one, which can be attributed to the buoyancy flux (Fig. 14d). It is also interesting to note that RF08 is the only flight with a minimum in  $\overline{w^2}$  being at the level above cloud base in the cloudy column relative to other MBL levels. This is most likely due to lower buoyancy production in the cloud layer of RF08 as compared to the other flights.

To further investigate the relative role of each buoyancy and shear term in the turbulence budget, the  $-z_i/L_{MO}$  ratio was compared between the two columns (Table 3). This ratio is an order of magnitude greater in the cloudy column as compared to clear one due to the latter column having stronger shear and reduced buoyancy flux. This confirms that shear is most likely the dominant mechanism for turbulence production in the clear column in the absence of the cloud layer.

### 3.4.2 RF09A and RF09B

The two flights on 3 August 2016 allowed for an opportunity to contrast clearing properties at two different times on the same day at roughly the same location (~20 km apart). Owing to their similarities, they are discussed together here. The clearing module in RF09A was performed between 11:00 and 12:30 PST, while that during RF09B was performed between 15:00 - 17:00 PST. Similar to RF08, MBL air in the clear column of RF09A and RF09B was slightly warmer than the cloudy column; however, the magnitude of the temperature difference (clear – cloudy) decreased from RF09A (~1.1K) to RF09B (~0.8K). SST was also greater by 0.4 K in the clear column of RF09A as compared to the cloud column, while it was slightly cooler by 0.1 K in the clear column of RF09B.

Specific humidity profiles in RF09A/RF09B exhibit more subtle differences as compared to RF08. In contrast to RF08, air in RF09A above the inversion base was drier and warmer in the region immediately above the inversion base and differences above the inversion base are less clear for RF09B. During both RF09A and RF09B, the clear profile exhibited steadily decreasing levels of water vapor with altitude, while the cloudy column was more well-mixed. The  $v$  component of wind speed again exhibited substantially greater values in the clear column as compared to the cloudy column for both RF09A and RF09B. Looking at the inversion layer properties (Table 3), the temperature gradient was lower and shear was greater in the clear column of RF09A and RF09B. Inversion depth was also greater in the clear column of RF09A, but less so for RF09B.



The sounding data in RF09A qualitatively resemble those from NiCE RF19 on 1 August 2013 where Crosbie et al. (2016) suspected that there was increased local subsidence and divergence in the clear column. Similar to their case, we observed the following in the clear column of RF09A: (i) warmer and drier air above and below the inversion base; (ii) the inversion base height was lower (354 m vs 375 m) with reduced temperature gradient in the inversion layer ( $0.33 \text{ K km}^{-1}$  vs  $0.41 \text{ K km}^{-1}$ ); and (iii) potential temperature exhibited warming and drying in the layer equivalent to the top 100 m of cloud. The RF09B case differed in that above the inversion base, the air in the clear column was not warmer and drier but very slightly cooler and moister, similar to RF08. This potentially is due to the diurnal nature of the clearing system where there is a stronger forcing to dissipate clouds during mid-day with the help of subsidence of dry and warm air from the FT, whereas later in the afternoon that process switches to a scenario where cooler and moister air exists above the inversion base and there is a waiting process for stronger radiative forcing to form a cloud again.

The cloud layer is the thickest in RF09A (191 m) among all three case flights. The cloud layer became thinner (137 m) later in the day during RF09B as a result of a change in the lifting condensation level (LCL), where cloud base increased from 217 m to 265 m. Moreover, LWP decreased during the day from  $32 \text{ g m}^{-2}$  to  $18 \text{ g m}^{-2}$ . It is important to note that the adiabaticity parameter, defined as the ratio of measured LWP to LWP of an adiabatic cloud, exhibited values of 0.75, 0.76, and 0.83 for RF08, RF09A, and RF09B, respectively. These adiabaticity values are close to the average value of 0.766 for the region reported in Braun et al. (2018). The clouds were quite thin near the interface based on the relatively low values of LWP in contrast to typical conditions observed in the region based on airborne measurements in the same campaigns (Fig. 3 of Sorooshian et al., 2019). Other cloud properties such as  $N_d$ ,  $r_e$ , and rain rate were quite similar in both RF09A and RF09B.  $N_d$  was greater in RF09A and RF09B as compared to RF08, corresponding to smaller values of  $r_e$  and suppressed drizzle. The dataset cannot provide unambiguous evidence as to whether the higher surface aerosol concentrations in RF09A and RF09B, as compared to RF08, were due to (or led to) suppressed drizzle.

Profiles of  $\overline{u^2}$  and  $\overline{v^2}$  exhibited downward trends with increasing altitude for RF09A and RF09B, in general agreement with the findings for RF08. One contrasting aspect was the comparison of  $\overline{v^2}$  between clear and cloudy columns, which mirrored RF08 during RF09A, while in RF09B, the values of  $\overline{v^2}$  for the clear side were substantially lower. In addition,  $\overline{w^2}$  profiles during RF09A and RF09B are substantially enhanced in the cloudy column as compared to RF08, with maxima in the cloud layer. There is an accompanying increase in the buoyancy flux for these profiles suggestive of a more significant contribution of buoyancy to TKE production. Although more subtle,  $\overline{u^2}$  values also showed an increase in the cloudy columns of RF09A and RF09B, also supportive of the role of buoyancy in these cases. Drizzle may be an important factor in governing the differences in buoyancy between the cloudy columns of RF09A/B and RF08, by creating a stabilizing effect. While no obvious decoupling of the RF08 cloudy MBL is observed, this profile may rely more heavily on shear production to maintain a well-mixed state. The clearing persisted following RF08, while there was a rapid infilling of cloud during the night following RF09A/B, similar to the case presented by Crosbie et al. (2016), which was also non-drizzling. While the nocturnal radiative environment has been shown to be conducive to infilling of clearings, we hypothesize that other factors that promote tighter coupling between the cloud layer and the surface (such as a lack of drizzle) may also contribute.



#### 4 Conclusions

This study extends upon recent works interested in large stratocumulus clearings that significantly impact albedo and have implications for fog, cloud, and weather forecasting. We specifically reported on ten years (2009-2018) of satellite and reanalysis data to characterize the temporal behavior, spatial and dimensional characteristics, growth rates, and governing environmental properties controlling the growth of clearings off the U.S. West Coast. We also examined three case flights from the 2016 FASE campaign that probed clearings to gain a deeper insight at finer spatial scales to try to validate speculated links between environmental parameters and clearing growth rates based on machine learning simulations using satellite and reanalysis data. The major results were as follows:

- (i) Summertime (wintertime) experiences the highest (lowest) frequency of clearings visible from space.
- (ii) The centroid of clearings is centered around coastal topographical features along the California coastline, specifically Cape Blanco and Cape Mendocino.
- (iii) The median length, width, and area of clearings between 09:00 and 18:00 (PST) increased from 680 km, 193 km, and ~67,000 km<sup>2</sup>, respectively, to ~1231 km, 443 km, and ~250,000 km<sup>2</sup>. The most growth occurred between 09:00-12:00.
- (iv) The most influential factors in clearing growth rates of total area between 09:00-12:00 were  $T_{850}$ ,  $q_{950}$ , SST, and  $V_{850}$ . Compared to non-clearing days, clearing days were characterized by having an enhanced Pacific high shifted more towards northern California, offshore air that is warm and dry, faster coastal surface winds, higher lower tropospheric static stability, and stronger subsidence.
- (v) Clearing days exhibited higher values of  $N_d$  and reduced values of  $r_e$ ,  $\tau$ , and LWP near the California coast where clearings form and evolve. However, the mean cloud albedo over the entire study domain was actually higher on clearing days.
- (vi) Airborne data revealed that extensive horizontal shear at cloud-relevant altitudes, with much faster winds parallel to the clearing edge on the clear side as compared to the cloudy side. This helped to promote mixing and thus dissipation of clouds. Differences in sounding profiles reveal that warm and dry air in the free troposphere additionally promoted expansion of clearings.

More research is needed to further characterize clearings and the broader regions they evolve in. For instance, it remains uncertain as to if there is a physical link between the existence of clearings and a higher domain-wide cloud albedo on clearing days. More data can help understand processes occurring at the microscale that scale up to more climatologically relevant scales. The results of this work showed that there are important diurnal features that require additional examination with in situ observations. One of the hypotheses posed in this work requiring more measurements and statistical robustness is the link between sea salt aerosol and the formation and evolution of clearing events. Clearing days are characterized by having stronger northerly winds, which translate into higher sea spray fluxes, which subsequently can impact clouds via faster onset of drizzle. This chain of events subsequently can thin out clouds via depletion of cloud water. Targeted experiments to examine these types of events will help advance understanding about their nature, which can then be contrasted with clearings along other coastal regions such as the





southeastern Atlantic Ocean. Also, the nature of clearings has direct relevance to CTD events that evolve in similar regions as discussed by Juliano et al. (2019a,b).

#### **Data availability**

Airborne field data used in this work can be found on the Figshare database (Sorooshian et al., 2017; [https://figshare.com/articles/A\\_Multi-Year\\_Data\\_Set\\_on\\_Aerosol-Cloud-Precipitation-Meteorology\\_Interactions\\_for\\_Marine\\_Stratocumulus\\_Clouds/5099983](https://figshare.com/articles/A_Multi-Year_Data_Set_on_Aerosol-Cloud-Precipitation-Meteorology_Interactions_for_Marine_Stratocumulus_Clouds/5099983)). Also, the satellite and reanalysis data used can be obtained from websites listed in Sections 2.1-2.2.

#### **Author contributions**

EC, XZ, and AS designed the study. HJ, AS, EC, and HD conducted research flights in FASE field campaign. MSM and HD developed the image analysis tool to analyze GOES images. MP, HD, and MAM conducted the GBRT model. HD analyzed the collected data. AB, MB, and XZ provided inputs for various part of project. AS and HD wrote the paper. EC, MAM, AB, MB, and XZ revised the manuscript.

#### **Competing interests**

The authors declare that they have no conflict of interest.

#### **Acknowledgments**

This work was funded by Office of Naval Research grant N00014-16-1-2567 and NASA grants NNX14AM02G and 80NSSC19K0442, the latter of which is in support of the ACTIVATE Earth Venture Suborbital-3 (EVS-3) investigation, which is funded by NASA's Earth Science Division and managed through the Earth System Science Pathfinder Program Office.





## References

- Albrecht, B. A.: Parameterization of Trade-Cumulus Cloud Amounts, *J Atmos Sci*, 38, 97-105, Doi 10.1175/1520-0469, 1981.
- Albrecht, B. A., Jensen, M. P., and Syrett, W. J.: Marine Boundary-Layer Structure and Fractional Cloudiness, *J Geophys Res-Atmos*, 100, 14209-14222, Doi 10.1029/95jd00827, 1995.
- Bennartz, R.: Global assessment of marine boundary layer cloud droplet number concentration from satellite, *J Geophys Res-Atmos*, 112, Artn D02201, 10.1029/2006jd007547, 2007.
- Braun, R. A., Dadashazar, H., MacDonald, A. B., Crosbie, E., Jonsson, H. H., Woods, R. K., Flagan, R. C., Seinfeld, J. H., and Sorooshian, A.: Cloud Adiabaticity and Its Relationship to Marine Stratocumulus Characteristics Over the Northeast Pacific Ocean, *J Geophys Res-Atmos*, 123, 13790-13806, 10.1029/2018JD029287, 2018.
- Bretherton, C. S., Klinker, E., Betts, A. K., and Coakley, J. A.: Comparison of Ceilometer, Satellite, and Synoptic Measurements of Boundary-Layer Cloudiness and the ECMWF Diagnostic Cloud Parameterization Scheme during ASTEX, *J Atmos Sci*, 52, 2736-2751, Doi 10.1175/1520-0469, 1995.
- Bretherton, C. S., Blossey, P. N., and Jones, C. R.: Mechanisms of marine low cloud sensitivity to idealized climate perturbations: A single-LES exploration extending the CGILS cases, *J Adv Model Earth Sy*, 5, 316-337, 10.1002/jame.20019, 2013.
- Brueck, M., Nuijens, L., and Stevens, B.: On the Seasonal and Synoptic Time-Scale Variability of the North Atlantic Trade Wind Region and Its Low-Level Clouds, *J Atmos Sci*, 72, 1428-1446, 10.1175/Jas-D-14-0054.1, 2015.
- Brunke, M. A., Ma, P.-L., Reeves Eyre, J. E. J., Rasch, P. J., Sorooshian, A., and Zeng, X.: Subtropical marine low stratiform cloud deck spatial errors in the E3SMv1 Atmosphere Model. *Geophys Res-Letters*, 46, 10.1029/2019GL084747, 2019.
- Bosilovich, M. G., Lucchesi, R., and Suarez, M.: MERRA-2: File specification. GMAO Office Note No. 9 (Version 1.1), 73 pp, 2016, available from [http://gmao.gsfc.nasa.gov/pubs/office\\_notes](http://gmao.gsfc.nasa.gov/pubs/office_notes).
- Coakley, J. A., Durkee, P. A., Nielsen, K., Taylor, J. P., Platnick, S., Albrecht, B. A., Babb, D., Chang, F. L., Tahnk, W. R., Bretherton, C. S., and Hobbs, P. V.: The appearance and disappearance of ship tracks on large spatial scales, *J Atmos Sci*, 57, 2765-2778, Doi 10.1175/1520-0469, 2000.
- Coggon, M. M., Sorooshian, A., Wang, Z., Craven, J. S., Metcalf, A. R., Lin, J. J., Nenes, A., Jonsson, H. H., Flagan, R. C., and Seinfeld, J. H.: Observations of continental biogenic impacts on marine aerosol and clouds off the coast of California, *J Geophys Res-Atmos*, 119, 6724-6748, 10.1002/2013JD021228, 2014.



- 883 Crosbie, E., Wang, Z., Sorooshian, A., Chuang, P. Y., Craven, J. S., Coggon, M. M., Brunke, M.,  
 884 Zeng, X. B., Jonsson, H., Woods, R. K., Flagan, R. C., and Seinfeld, J. H.: Stratocumulus Cloud  
 885 Clearings and Notable Thermodynamic and Aerosol Contrasts across the Clear-Cloudy Interface,  
 886 J Atmos Sci, 73, 1083-1099, 10.1175/Jas-D-15-0137.1, 2016.
- 887  
 888 Crosbie, E., Brown, M. D., Shook, M., Ziemba, L., Moore, R. H., Shingler, T., Winstead, E.,  
 889 Thornhill, K. L., Robinson, C., MacDonald, A. B., Dadashazar, H., Sorooshian, A., Beyersdorf,  
 890 A., Eugene, A., Collett, J., Straub, D., and Anderson, B.: Development and characterization of a  
 891 high-efficiency, aircraft-based axial cyclone cloud water collector, Atmos Meas Tech, 11, 5025-  
 892 5048, 10.5194/amt-11-5025-2018, 2018.
- 893  
 894 Dadashazar, H., Wang, Z., Crosbie, E., Brunke, M., Zeng, X. B., Jonsson, H., Woods, R. K.,  
 895 Flagan, R. C., Seinfeld, J. H., and Sorooshian, A.: Relationships between giant sea salt particles  
 896 and clouds inferred from aircraft physicochemical data, J Geophys Res-Atmos, 122, 3421-3434,  
 897 10.1002/2016JD026019, 2017.
- 898  
 899 Durkee, P. A., Noone, K. J., Ferek, R. J., Johnson, D. W., Taylor, J. P., Garrett, T. J., Hobbs, P.  
 900 V., Hudson, J. G., Bretherton, C. S., Innis, G., Frick, G. M., Hoppel, W. A., O'Dowd, C. D.,  
 901 Russell, L. M., Gasparovic, R., Nielsen, K. E., Tessmer, S. A., Ostrom, E., Osborne, S. R., Flagan,  
 902 R. C., Seinfeld, J. H., and Rand, H.: The impact of ship-produced aerosols on the microstructure  
 903 and albedo of warm marine stratocumulus clouds: A test of MAST hypotheses Ii and Iii, J Atmos  
 904 Sci, 57, 2554-2569, Doi 10.1175/1520-0469, 2000.
- 905  
 906 Friedman, J. H.: Greedy function approximation: A gradient boosting machine, Ann Stat, 29(5),  
 907 1189-1232, 2001.
- 908  
 909 Fuchs, J., Cermak, J., and Andersen, H.: Building a cloud in the southeast Atlantic: understanding  
 910 low-cloud controls based on satellite observations with machine learning, Atmos Chem Phys, 18,  
 911 16537-16552, 10.5194/acp-18-16537-2018, 2018.
- 912  
 913 Gelaro, R., McCarty, W., Suarez, M. J., Todling, R., Molod, A., Takacs, L., Randles, C. A.,  
 914 Darmenov, A., Bosilovich, M. G., Reichle, R., Wargan, K., Coy, L., Cullather, R., Draper, C.,  
 915 Akella, S., Buchard, V., Conaty, A., da Silva, A. M., Gu, W., Kim, G. K., Koster, R., Lucchesi,  
 916 R., Merkova, D., Nielsen, J. E., Partyka, G., Pawson, S., Putman, W., Rienecker, M., Schubert, S.  
 917 D., Sienkiewicz, M., and Zhao, B.: The Modern-Era Retrospective Analysis for Research and  
 918 Applications, Version 2 (MERRA-2), J Climate, 30, 5419-5454, 10.1175/Jcli-D-16-0758.1, 2017.
- 919  
 920 Gerber, H., Arends, B. G., and Ackerman, A. S.: New microphysics sensor for aircraft use, Atmos  
 921 Res, 31, 235-252, Doi 10.1016/0169-8095(94)90001-9, 1994.
- 922  
 923 Hahn, C. J., and S. G. Warren: A gridded climatology of clouds over land (1971–96) and ocean  
 924 (1954–97) from surface observations worldwide. Numeric Data Package NDP-026E  
 925 ORNL/CDIAC-153, CDIAC, Department of Energy, Oak Ridge, TN, 2007.
- 926  
 927 Hegg, D. A., and P. V. Hobbs (1986), Studies of the mechanisms and rate with which nitrogen  
 928 species are incorporated into cloud water and precipitation, Second Annual Report on Project  
 929 CAPA-21-80 to the Coordinating Research Council.



- 930  
 931 Hegg, D. A., Covert, D. S., Jonsson, H. H., and Woods, R. K.: The contribution of anthropogenic  
 932 aerosols to aerosol light-scattering and CCN activity in the California coastal zone, *Atmos Chem*  
 933 *Phys*, 10, 7341-7351, 10.5194/acp-10-7341-2010, 2010.
- 934  
 935 Hubanks, P. A., King, M. D., Platnick, S., and Pincus, R.: MODIS atmosphere L3 gridded product  
 936 algorithm theoretical basis document, ATBD Reference Number: ATBD-MOD-30, 2019.
- 937  
 938 Juliano, T. W., Parish, T. R., Rahn, D. A., and Leon, D. C.: An Atmospheric Hydraulic Jump in  
 939 the Santa Barbara Channel, *J Appl Meteorol Clim*, 56, 2981-2998, 10.1175/Jamc-D-16-0396.1,  
 940 2017.
- 941  
 942 Juliano, T. W., Lebo, Z. J., Thompson, G., and Rahn, D. A.: A New Perspective on Coastally  
 943 Trapped Disturbances Using Data from the Satellite Era, *B Am Meteorol Soc*, 100, 631-651,  
 944 10.1175/Bams-D-18-0002.1, 2019a.
- 945  
 946 Juliano, T. W., Coggon, M. M., Thompson, G., Rahn, D. A., Seinfeld, J. H., Sorooshian, A., and  
 947 Lebo, Z. J.: Marine Boundary Layer Clouds Associated with Coastally Trapped Disturbances:  
 948 Observations and Model Simulations, *J Atmos Sci*, 76, 2963-2993, 10.1175/Jas-D-18-0317.1,  
 949 2019b.
- 950  
 951 Jung, E., Albrecht, B. A., Jonsson, H. H., Chen, Y. C., Seinfeld, J. H., Sorooshian, A., Metcalf, A.  
 952 R., Song, S., Fang, M., and Russell, L. M.: Precipitation effects of giant cloud condensation nuclei  
 953 artificially introduced into stratocumulus clouds, *Atmos Chem Phys*, 15, 5645-5658, 10.5194/acp-  
 954 15-5645-2015, 2015.
- 955  
 956 Klein, S. A.: Synoptic variability of low-cloud properties and meteorological parameters in the  
 957 subtropical trade wind boundary layer, *J Climate*, 10, 2018-2039, Doi 10.1175/1520-0442, 1997.
- 958  
 959 Klein, S. A., and Hartmann, D. L.: The Seasonal Cycle of Low Stratiform Clouds, *J Climate*, 6,  
 960 1587-1606, Doi 10.1175/1520-0442, 1993.
- 961  
 962 Klein, S. A., Hartmann, D. L., and Norris, J. R.: On the Relationships among Low-Cloud Structure,  
 963 Sea-Surface Temperature, and Atmospheric Circulation in the Summertime Northeast Pacific, *J*  
 964 *Climate*, 8, 1140-1155, Doi 10.1175/1520-0442, 1995.
- 965  
 966 Kloesel, K. A.: Marine Stratocumulus Cloud Clearing Episodes Observed during Fire, *Mon*  
 967 *Weather Rev*, 120, 565-578, Doi 10.1175/1520 0493, 1992.
- 968  
 969 Lacis, A. A., and Hansen, J. E.: Parameterization for Absorption of Solar-Radiation in Earths  
 970 Atmosphere, *J Atmos Sci*, 31, 118-133, Doi 10.1175/1520-0469, 1974.
- 971  
 972 Lu, M. L., Sorooshian, A., Jonsson, H. H., Feingold, G., Flagan, R. C., and Seinfeld, J. H.: Marine  
 973 stratocumulus aerosol-cloud relationships in the MASE-II experiment: Precipitation susceptibility  
 974 in eastern Pacific marine stratocumulus, *J Geophys Res-Atmos*, 114, ArtId  
 975 D24203, 10.1029/2009jd012774, 2009.



976  
 977 MacDonald, A. B., Dadashazar, H., Chuang, P. Y., Crosbie, E., Wang, H. L., Wang, Z., Jonsson,  
 978 H. H., Flagan, R. C., Seinfeld, J. H., and Sorooshian, A.: Characteristic Vertical Profiles of Cloud  
 979 Water Composition in Marine Stratocumulus Clouds and Relationships With Precipitation, *J*  
 980 *Geophys Res-Atmos*, 123, 3704-3723, 10.1002/2017JD027900, 2018.  
 981  
 982 Mardi, A. H., Dadashazar, H., MacDonald, A. B., Braun, R. A., Crosbie, E., Xian, P., Thorsen, T.  
 983 J., Coggon, M. M., Fenn, M. A., Ferrare, R. A., Hair, J. W., Woods, R. K., Jonsson, H. H., Flagan,  
 984 R. C., Seinfeld, J. H., and Sorooshian, A.: Biomass Burning Plumes in the Vicinity of the  
 985 California Coast: Airborne Characterization of Physicochemical Properties, Heating Rates, and  
 986 Spatiotemporal Features, *J Geophys Res-Atmos*, 123, 13560-13582, 10.1029/2018JD029134,  
 987 2018.  
 988  
 989 Martin, G. M., Johnson, D. W., and Spice, A.: The Measurement and Parameterization of Effective  
 990 Radius of Droplets in Warm Stratocumulus Clouds, *J Atmos Sci*, 51, 1823-1842, Doi  
 991 10.1175/1520-0469, 1994.  
 992  
 993 Maudlin, L. C., Wang, Z., Jonsson, H. H., and Sorooshian, A.: Impact of wildfires on size-resolved  
 994 aerosol composition at a coastal California site, *Atmos Environ*, 119, 59-68,  
 995 10.1016/j.atmosenv.2015.08.039, 2015.  
 996  
 997 Myers, T. A., and Norris, J. R.: Observational Evidence That Enhanced Subsidence Reduces  
 998 Subtropical Marine Boundary Layer Cloudiness, *J Climate*, 26, 7507-7524, 10.1175/Jcli-D-12-  
 999 00736.1, 2013.  
 1000  
 1001 McCoy, D. T., Bender, F. A. M., Mohrmann, J. K. C., Hartmann, D. L., Wood, R., and Grosvenor,  
 1002 D. P.: The global aerosol-cloud first indirect effect estimated using MODIS, MERRA, and  
 1003 AeroCom, *J Geophys Res-Atmos*, 122, 1779-1796, 10.1002/2016JD026141, 2017.  
 1004  
 1005 Menzel, W. P., and Purdom, J. F. W.: Introducing GOES-1: The first of a new generation of  
 1006 geostationary operational environmental satellites, *Bull. Amer. Meteor. Soc.*, 75, 757-781, 1994.  
 1007  
 1008 Modini, R. L., Frossard, A. A., Ahlm, L., Russell, L. M., Corrigan, C. E., Roberts, G. C., Hawkins,  
 1009 L. N., Schroder, J. C., Bertram, A. K., Zhao, R., Lee, A. K. Y., Abbatt, J. P. D., Lin, J., Nenes, A.,  
 1010 Wang, Z., Wonaschutz, A., Sorooshian, A., Noone, K. J., Jonsson, H., Seinfeld, J. H., Toom-  
 1011 Saunty, D., Macdonald, A. M., and Leaitch, W. R.: Primary marine aerosol-cloud interactions off  
 1012 the coast of California, *J Geophys Res-Atmos*, 120, 4282-4303, 10.1002/2014JD022963, 2015.  
 1013  
 1014 Norris, J. R., and Leovy, C. B.: Interannual Variability in Stratiform Cloudiness and Sea-Surface  
 1015 Temperature, *J Climate*, 7, 1915-1925, Doi 10.1175/1520-0442, 1994.  
 1016  
 1017 Nicholls, S., and Leighton, J.: An observational study of the structure of stratiform cloud sheets:  
 1018 Part I. Structure. *Quart. J. Roy. Meteor. Soc.*, 112, 431-460, 1986.  
 1019  
 1020 Otsu, N., "A Threshold Selection Method from Gray-Level Histograms." *IEEE Transactions on*  
 1021 *Systems, Man, and Cybernetics*. Vol. 9, No. 1, pp. 62-66, 1979.



- 1022
- 1023 Painemal, D., and Zuidema, P.: Microphysical variability in southeast Pacific Stratocumulus
- 1024 clouds: synoptic conditions and radiative response, *Atmos Chem Phys*, 10, 6255-6269,
- 1025 10.5194/acp-10-6255-2010, 2010.
- 1026
- 1027 Painemal, D., and Minnis, P.: On the dependence of albedo on cloud microphysics over marine
- 1028 stratocumulus clouds regimes determined from Clouds and the Earth's Radiant Energy System
- 1029 (CERES) data (vol 117, D06203, 2012), *J Geophys Res-Atmos*, 117, ArtId
- 1030 D09299, 10.1029/2012jd017902, 2012.
- 1031
- 1032 Pedregosa, F., Varoquaux, G., Gramfort, A., Michel, V., Thirion, B., Grisel, O., Blondel, M.,
- 1033 Prettenhofer, P., Weiss, R., Dubourg, V., Vanderplas, J., Passos, A., Cournapeau, D., Brucher, M.,
- 1034 Perrot, M., and Duchesnay, E.: Scikit-learn: Machine Learning in Python, *J Mach Learn Res*, 12,
- 1035 2825-2830, 2011.
- 1036
- 1037 Platnick, S., King, M. D., Ackerman, S. A., Menzel, W. P., Baum, B. A., Riedi, J. C., and Frey, R.
- 1038 A.: The MODIS cloud products: Algorithms and examples from Terra, *Ieee T Geosci Remote*, 41,
- 1039 459-473, 10.1109/Tgrs.2002.808301, 2003.
- 1040
- 1041 Platnick, S., Meyer, K. G., King, M. D., Wind, G., Amarasinghe, N., Marchant, B., Arnold, G. T.,
- 1042 Zhang, Z. B., Hubanks, P. A., Holz, R. E., Yang, P., Ridgway, W. L., and Riedi, J.: The MODIS
- 1043 Cloud Optical and Microphysical Products: Collection 6 Updates and Examples From Terra and
- 1044 Aqua, *Ieee T Geosci Remote*, 55, 502-525, 10.1109/Tgrs.2016.2610522, 2017.
- 1045
- 1046 Prabhakar, G., Ervens, B., Wang, Z., Maudlin, L. C., Coggon, M. M., Jonsson, H. H., Seinfeld, J.
- 1047 H., and Sorooshian, A.: Sources of nitrate in stratocumulus cloud water: Airborne measurements
- 1048 during the 2011 E-PEACE and 2013 NiCE studies, *Atmos Environ*, 97, 166-173,
- 1049 10.1016/j.atmosenv.2014.08.019, 2014.
- 1050
- 1051 Russell, L. M., Sorooshian, A., Seinfeld, J. H., Albrecht, B. A., Nenes, A., Ahlm, L., Chen, Y. C.,
- 1052 Coggon, M., Craven, J. S., Flagan, R. C., Frossard, A. A., Jonsson, H., Jung, E., Lin, J. J., Metcalf,
- 1053 A. R., Modini, R., Mulmenstadt, J., Roberts, G. C., Shingler, T., Song, S., Wang, Z., and
- 1054 Wonaschutz, A.: Eastern Pacific Emitted Aerosol Cloud Experiment, *B Am Meteorol Soc*, 94,
- 1055 709-+, 10.1175/Bams-D-12-00015.1, 2013.
- 1056
- 1057 Sanchez, K. J., Russell, L. M., Modini, R. L., Frossard, A. A., Ahlm, L., Corrigan, C. E., Roberts,
- 1058 G. C., Hawkins, L. N., Schroder, J. C., Bertram, A. K., Zhao, R., Lee, A. K. Y., Lin, J. J., Nenes,
- 1059 A., Wang, Z., Wonaschutz, A., Sorooshian, A., Noone, K. J., Jonsson, H., Toom, D., Macdonald,
- 1060 A. M., Leaitch, W. R., and Seinfeld, J. H.: Meteorological and aerosol effects on marine cloud
- 1061 microphysical properties, *J Geophys Res-Atmos*, 121, 4142-4161, 10.1002/2015JD024595, 2016.
- 1062
- 1063 Sorooshian, A., Wang, Z., Coggon, M. M., Jonsson, H. H., and Ervens, B.: Observations of Sharp
- 1064 Oxalate Reductions in Stratocumulus Clouds at Variable Altitudes: Organic Acid and Metal
- 1065 Measurements During the 2011 E-PEACE Campaign, *Environ Sci Technol*, 47, 7747-7756,
- 1066 10.1021/es4012383, 2013a.
- 1067



- 1068 Sorooshian, A., Wang, Z., Feingold, G., and L'Ecuyer, T. S.: A satellite perspective on cloud water  
 1069 to rain water conversion rates and relationships with environmental conditions, *J Geophys Res-*  
 1070 *Atmos*, 118, 6643-6650, 10.1002/jgrd.50523, 2013b.
- 1071
- 1072 Sorooshian, A., MacDonald, A. B., Dadashazar, H., Bates, K. H., Coggon, M. M., Craven, J. S.,  
 1073 Crosbie, E., Hersey, S. P., Hodas, N., Lin, J. J., Marty, A. N., Maudlin, L. C., Metcalf, A. R.,  
 1074 Murphy, S. M., Padro, L. T., Prabhakar, G., Rissman, T. A., Shingler, T., Varutbangkul, V., Wang,  
 1075 Z., Woods, R. K., Chuang, P. Y., Nenes, A., Jonsson, H. H., Flagan, R. C., and Seinfeld, J. H.: A  
 1076 multi-year data set on aerosol-cloud-precipitation-meteorology interactions for marine  
 1077 stratocumulus clouds, Figshare, <https://doi.org/10.6084/m9.figshare.5099983.v3>, 2017.
- 1078
- 1079 Sorooshian, A., MacDonald, A. B., Dadashazar, H., Bates, K. H., Coggon, M. M., Craven, J. S.,  
 1080 Crosbie, E., Hersey, S. P., Hodas, N., Lin, J. J., Marty, A. N., Maudlin, L. C., Metcalf, A. R.,  
 1081 Murphy, S. M., Padro, L. T., Prabhakar, G., Rissman, T. A., Shingler, T., Varutbangkul, V., Wang,  
 1082 Z., Woods, R. K., Chuang, P. Y., Nenes, A., Jonsson, H. H., Flagan, R. C., and Seinfeld, J. H.: A  
 1083 multi-year data set on aerosol-cloud-precipitation-meteorology interactions for marine  
 1084 stratocumulus clouds, *Sci Data*, 5, Artn 180026, 10.1038/Sdata.2018.26, 2018.
- 1085
- 1086 Sorooshian, A., Anderson, B., Bauer, S. E., Braun, R. A., Cairns, B., Crosbie, E., Dadashazar, H.,  
 1087 Diskin, G., Ferrare, R., Flagan, R. C., Hair, J., Hostetler, C., Jonsson, H. H., Kleb, M. M., Liu, H.  
 1088 Y., MacDonald, A. B., McComiskey, A., Moore, R., Painemal, D., Russell, L. M., Seinfeld, J. H.,  
 1089 Shook, M., Smith, W. L., Thornhill, K., Tselioudis, G., Wang, H. L., Zeng, X. B., Zhang, B.,  
 1090 Ziemba, L., and Zuidema, P.: Aerosol-Cloud-Meteorology Interaction Airborne Field  
 1091 Investigations: Using Lessons Learned from the US West Coast in the Design of ACTIVATE off  
 1092 the US East Coast, *B Am Meteorol Soc*, 100, 1511-1528, 10.1175/Bams-D-18-0100.1, 2019.
- 1093
- 1094 Stevens, B., Lenschow, D. H., Vali, G., Gerber, H., Bandy, A., Blomquist, B., Brenguier, J. L.,  
 1095 Bretherton, C. S., Burnet, F., Campos, T., Chai, S., Faloona, I., Friesen, D., Haimov, S., Laursen,  
 1096 K., Lilly, D. K., Loehrer, S. M., Malinowski, S. P., Morley, B., Petters, M. D., Rogers, D. C.,  
 1097 Russell, L., Savic-Jovac, V., Snider, J. R., Straub, D., Szumowski, M. J., Takagi, H., Thornton, D.  
 1098 C., Tschudi, M., Twohy, C., Wetzol, M., and van Zanten, M. C.: Dynamics and chemistry of  
 1099 marine stratocumulus - Dycoms-II, *B Am Meteorol Soc*, 84, 579-593, 10.1175/Bams-84-5-579,  
 1100 2003.
- 1101
- 1102 Stull, R. B.: *An Introduction to Boundary Layer Meteorology*. Kluwer Academic, 666 pp, 1988.
- 1103
- 1104 Tibshirani, R.: Regression shrinkage and selection via the Lasso, *J Roy Stat Soc B Met*, 58(1), 267-  
 1105 288, 1996.
- 1106
- 1107 Wang, S. P., Albrecht, B. A., and Minnis, P.: A Regional Simulation of Marine Boundary-Layer  
 1108 Clouds, *J Atmos Sci*, 50, 4022-4043, Doi 10.1175/1520-0469, 1993.
- 1109
- 1110 Wang, Z., Sorooshian, A., Prabhakar, G., Coggon, M. M., and Jonsson, H. H.: Impact of emissions  
 1111 from shipping, land, and the ocean on stratocumulus cloud water elemental composition during  
 1112 the 2011 E-PEACE field campaign, *Atmos Environ*, 89, 570-580,  
 1113 10.1016/j.atmosenv.2014.01.020, 2014.





- 1114  
 1115 Wang, Z., Ramirez, M. M., Dadashazar, H., MacDonald, A. B., Crosbie, E., Bates, K. H., Coggon,  
 1116 M. M., Craven, J. S., Lynch, P., Campbell, J. R., Aghdam, M. A., Woods, R. K., Jonsson, H.,  
 1117 Flagan, R. C., Seinfeld, J. H., and Sorooshian, A.: Contrasting cloud composition between coupled  
 1118 and decoupled marine boundary layer clouds, *J Geophys Res-Atmos*, 121, 11679-11691,  
 1119 10.1002/2016jd025695, 2016.
- 1120  
 1121 Warren, S. G., Hahn, C. J., London, J., Chervin, R. M., and Jenne, R. L.: Global distribution of  
 1122 total cloud cover and cloud types over land. NCAR Tech. Note NCAR/TN-2731STR, National  
 1123 Center for Atmospheric Research, Boulder, CO, 1986.
- 1124  
 1125 Wood, R.: Drizzle in stratiform boundary layer clouds. Part 1: Vertical and horizontal structure, *J*  
 1126 *Atmos Sci*, 62, 3011-3033, Doi 10.1175/Jas3529.1, 2005.
- 1127  
 1128 Wood, R., and Bretherton, C. S.: On the relationship between stratiform low cloud cover and  
 1129 lower-tropospheric stability, *J Climate*, 19, 6425-6432, Doi 10.1175/Jcli3988.1, 2006.
- 1130  
 1131 Youn, J. S., Crosbie, E., Maudlin, L. C., Wang, Z., and Sorooshian, A.: Dimethylamine as a major  
 1132 alkyl amine species in particles and cloud water: Observations in semi-arid and coastal regions,  
 1133 *Atmos Environ*, 122, 250-258, 10.1016/j.atmosenv.2015.09.061, 2015.
- 1134  
 1135 Yuter, S. E., Hader, J. D., Miller, M. A., and Mechem, D. B.: Abrupt cloud clearing of marine  
 1136 stratocumulus in the subtropical southeast Atlantic, *Science*, 361, 697-+, 10.1126/science.aar5836,  
 1137 2018.
- 1138  
 1139  
 1140



**Table 1.** Summary of reanalysis and satellite data products used in this study. For the rows with multiple products, underlined entries correspond to one in another between different columns.

Input coordinate for data download	Parameter	Source	Product identifier	Spatial resolution	Vertical level	Temporal resolution	Reference
20°-60° N, 110°-160° W	Visible band imagery	GOES-11/15 imager	NA	1 km × 1 km at nadir	NA	30 min	Menzel and Purdom, 1994
20°-60° N, 110°-160° W	Mean sea level pressure	MERRA-2 model	M2I3NPASM	0.5° × 0.625°	NA	3 h	Bosilovich et al., 2016
20°-60° N, 110°-160° W	Air temperature	MERRA-2 model	<u>M2T1NXFLX</u> / M2I3NPASM	0.5° × 0.625°	<u>Sea surface</u> , 950, 850, 700 hPa	<u>1 h</u> /3 h	Bosilovich et al., 2016
20°-60° N, 110°-160° W	Geopotential height	MERRA-2 model	M2I3NPASM	0.5° × 0.625°	850, 500 hPa	3 h	Bosilovich et al., 2016
20°-60° N, 110°-160° W	Wind speed	MERRA-2 model	M2T1NXFLX	0.5° × 0.625°	<u>Surface</u> , 950, 850, 700 hPa	<u>1 h</u> /3 h	Bosilovich et al., 2016
20°-60° N, 110°-160° W	Vertical pressure velocity	MERRA-2 model	M2I3NPASM	0.5° × 0.625°	700 hPa	3 h	Bosilovich et al., 2016
20°-60° N, 110°-160° W	Planetary boundary layer height	MERRA-2 model	M2T1NXFLX	0.5° × 0.625°	NA	1 h	Bosilovich et al., 2016
20°-60° N, 110°-160° W	Sea surface temperature	MERRA-2 model	M2T1NXOCN	0.5° × 0.625°	NA	1 h	Bosilovich et al., 2016
20°-60° N, 110°-160° W	Specific humidity	MERRA-2 model	<u>M2I1NXASM</u> /M2I3NPASM	0.5° × 0.625°	<u>10 m</u> , 950, 850, 700 hPa	<u>1 h</u> /3 h	Bosilovich et al., 2016
20°-60° N, 110°-160° W	Aerosol optical depth AOD	MERRA-2 model	M2I3NXGAS	0.5° × 0.625°	NA	3 h	Bosilovich et al., 2016
30°-50° N, 115°-135° W	Cloud optical thickness liquid	MODIS-Terra/Aqua	MOD08_D3/MYD08_D3	1° × 1°	NA	Daily	Hubanks et al., 2019
30°-50° N, 115°-135° W	Cloud fraction day	MODIS-Terra/Aqua	MOD08_D3/MYD08_D3	1° × 1°	NA	Daily	Hubanks et al., 2019
30°-50° N, 115°-135° W	Cloud water path liquid	MODIS-Terra/Aqua	MOD08_D3/MYD08_D3	1° × 1°	NA	Daily	Hubanks et al., 2019
30°-50° N, 115°-135° W	Cloud effective radius liquid	MODIS-Terra/Aqua	MOD08_D3/MYD08_D3	1° × 1°	NA	Daily	Hubanks et al., 2019



**Table 2.** Absolute changes in the parallel component of horizontal wind speed relative to the cloud edge,  $|\Delta v|$  in units of  $\text{m s}^{-1}$ , across various legs using FASE aircraft data. Values were calculated based on a 40 km leg distance (approximate length of each leg). Values for the cloud top leg were estimated using the sawtooth leg performed across the cloud top boundary. The free troposphere level leg was not conducted in RF08 and thus left blank.

	RF08	RF09A	RF09B
Free troposphere		0.4	1.6
Cloud top	9.6	6.4	4.8
Mid-cloud	7.2	6.8	6.0
Above cloud base	6.8	5.2	5.2
Surface	3.6	2.4	0.0



**Table 3.** Summary of thermodynamic, dynamic, and cloud properties on both sides of the clear-cloudy interface for three FASE case research flights (RFs).  $U$  represents total horizontal wind speed ( $U = \sqrt{u^2 + v^2}$ ) across the depth of the inversion layer.

	Cloudy			Clear		
	RF08	RF09A	RF09B	RF08	RF09A	RF09B
SST (K)	286.6	287.1	287.3	287.0	287.5	287.2
Surface wind ( $\text{m s}^{-1}$ )	11.3	11.1	11.6	13.2	12.3	11.5
$u^*$ ( $\text{m s}^{-1}$ )	0.15	0.19	0.11	0.40	0.32	0.25
$w^*$ ( $\text{m s}^{-1}$ )	0.44	0.64	0.68	0.44	0.53	0.38
$-Z_i/L_{MO}$	9.8	15.7	49.1	0.8	2.2	1.4
Inversion-base height (m)	367	375	391	359	354	386
Inversion-top height (m)	422	441	457	443	440	455
Inversion depth (m)	55	66	66	82	86	69
$\Delta\theta_i$ (K)	7.4	8.6	7.0	7.3	7.6	5.4
$(\Delta\theta_i/\Delta z)_{\text{Max}}$ ( $\text{K m}^{-1}$ )	0.38	0.41	0.25	0.32	0.33	0.23
$\Delta q_T$ ( $\text{g kg}^{-1}$ )	-3	-3.2	-2.6	-2.9	-3.3	-2.6
$\Delta U$ ( $\text{m s}^{-1}$ )	0.80	1.35	1.35	5.44	2.50	5.32
Cloud base (m)	242	217	265			
Cloud top (m)	372	408	401			
Cloud depth (m)	131	191	137			
Cloud LWP ( $\text{g m}^{-2}$ )	15	32	18			
$R_{cb}$ ( $\text{mm day}^{-1}$ )	0.48	0.09	0.07			
$r_e$ ( $\mu\text{m}$ )	6.6	6.0	5.9			
$N_d$ ( $\text{cm}^{-3}$ )	107	141	148			
Surface PCASP ( $\text{cm}^{-3}$ )	108	206	236	106	186	207

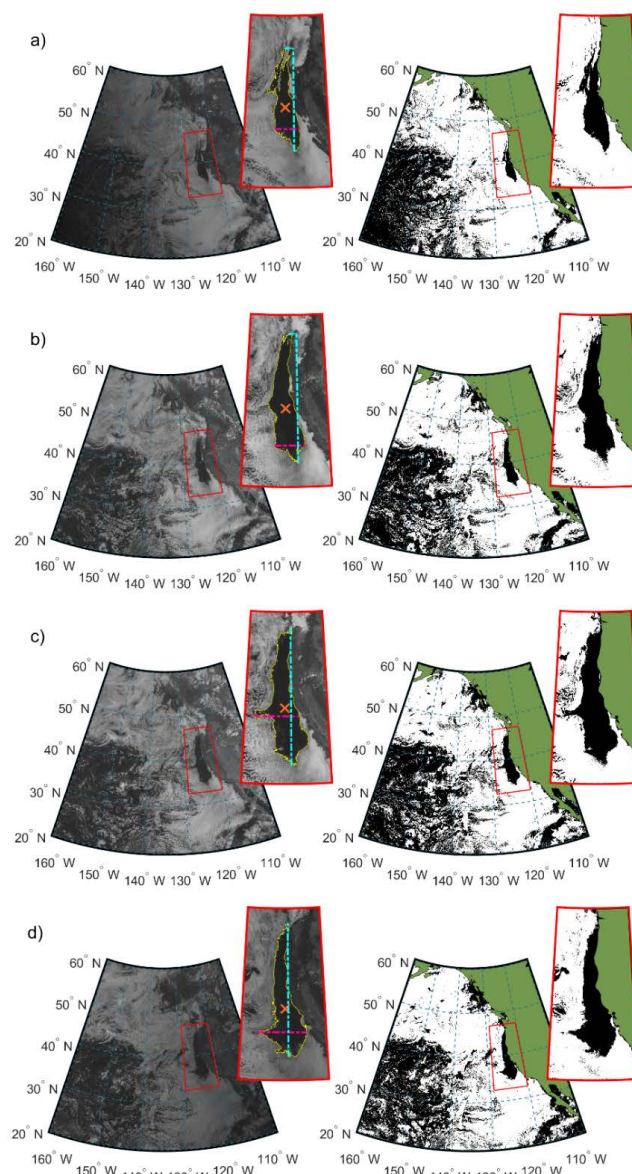


**Figure 1.** Sequence of data processing with GOES imagery at four times during a day: (i) 16:15 UTC 09 August 2011; (ii) 19:15 UTC 09 August 2011; (iii) 20:45 UTC 09 August 2011; and (iv) 01:15 UTC 10 August 2011. Left panels show visible-band images of a clearing event obtained from GOES-11 data, while the right panel is produced using cloud masking. Note that the clearing border, centroid, and lengths (x and y) are overlaid on the GOES images. Local time (PST) requires subtraction of seven hours from UTC time.

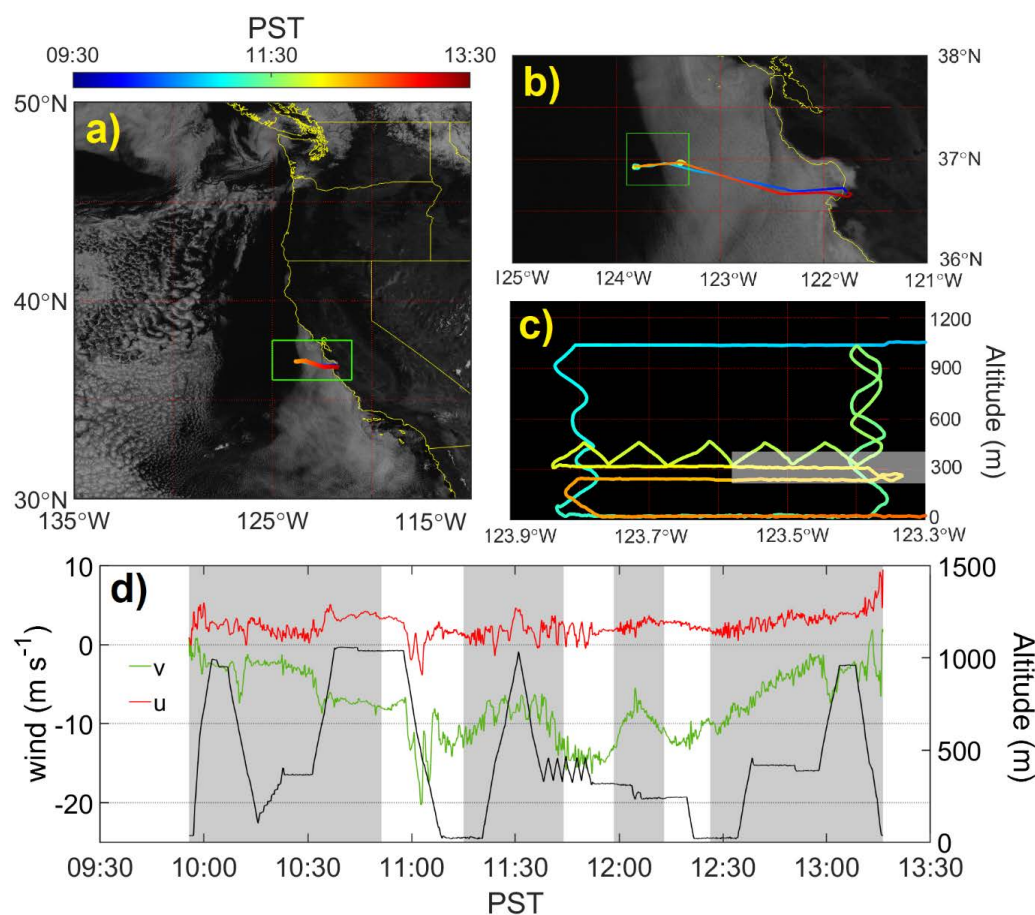


**Figure 2.** a) GOES 15 visible band image (11:45 (18:45) PST (UTC) on 03 Aug 2016) with the overlaid flight path of FASE RF09A. b) Zoomed-in view of the satellite image to highlight the clear-cloudy border. c) Aircraft flight strategy at the cloudy-clear interface for the green box highlighted in b). Cloud borders are denoted by a shaded box. d) Time series of flight altitude and horizontal wind speed, which is decomposed into two components that are perpendicular (u) and parallel (v) to the cloud edge. Wind speeds were smoothed using low-pass filtering. Parts of the flight that sampled air on the cloudy side of the clear-cloudy border are shaded in grey.



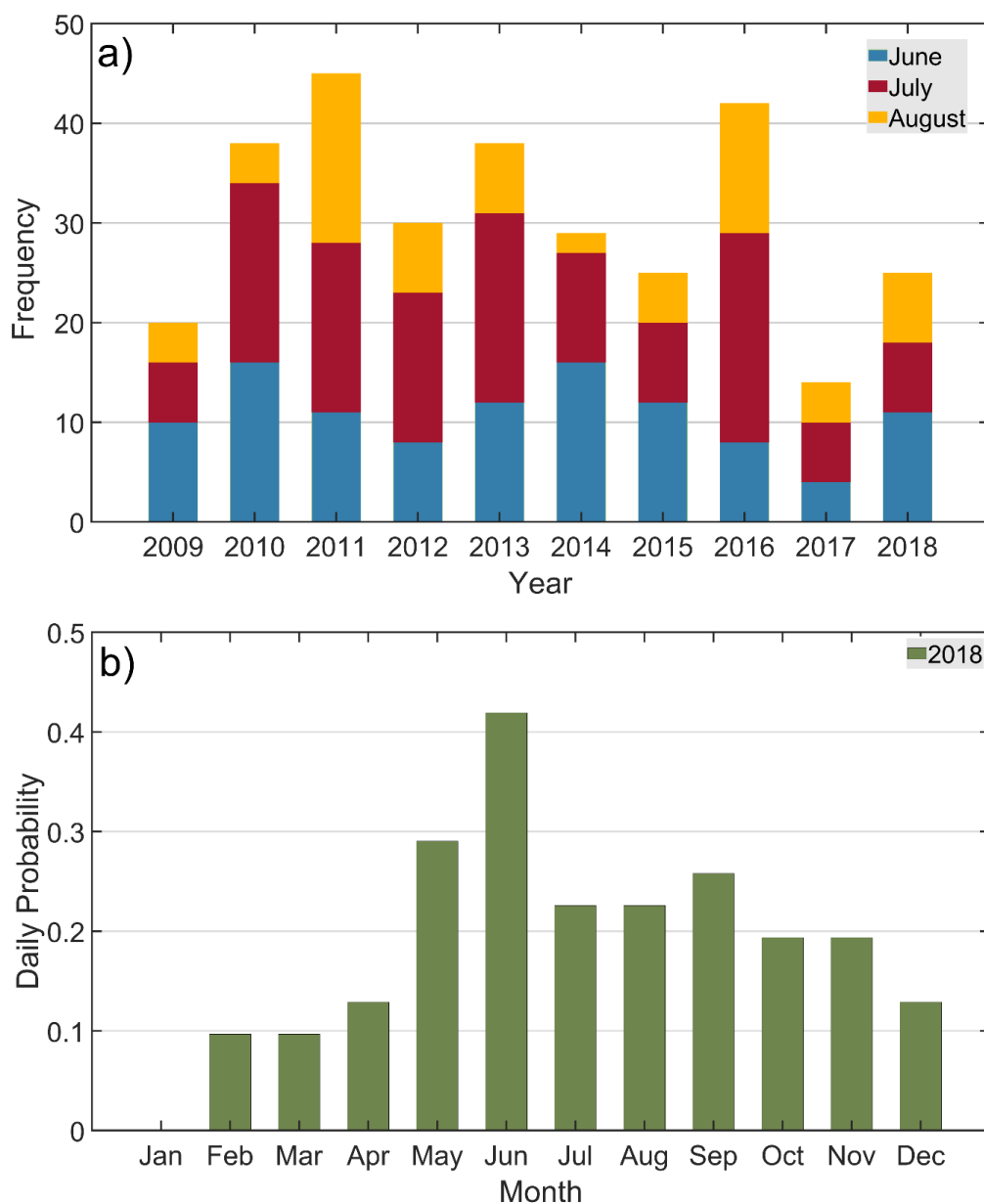


**Figure 3.** a) Frequency of clearing events in the study region for each summer month between 2009 and 2018. b) Daily probability of clearing events (i.e., days with clearings divided by total days in that month) in each month of a representative year, 2018.

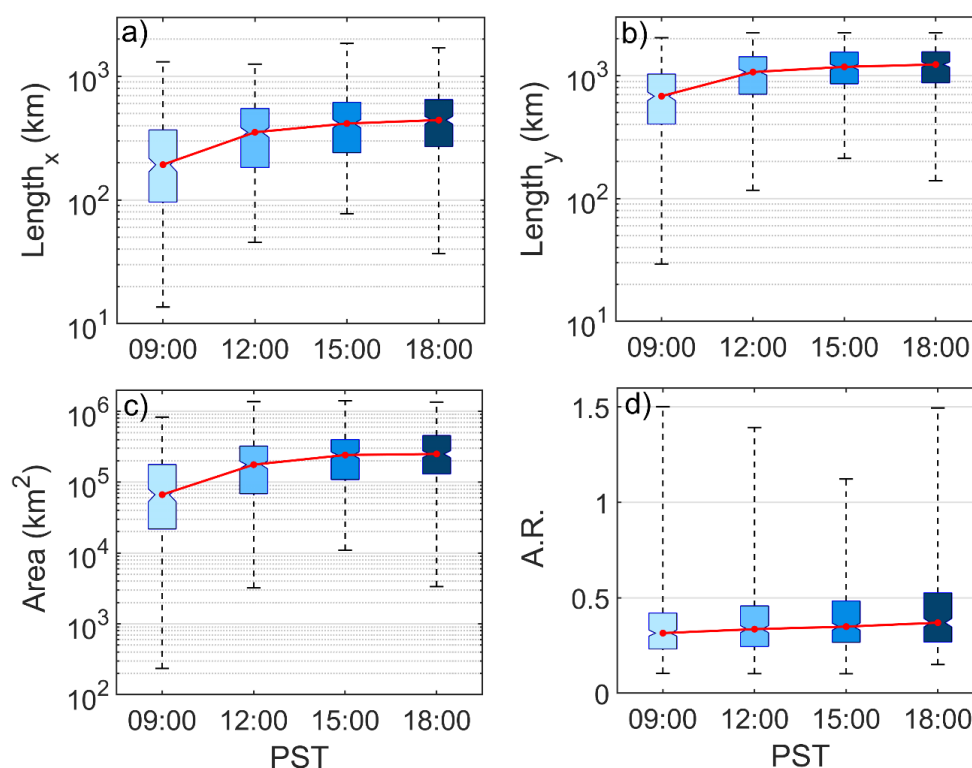
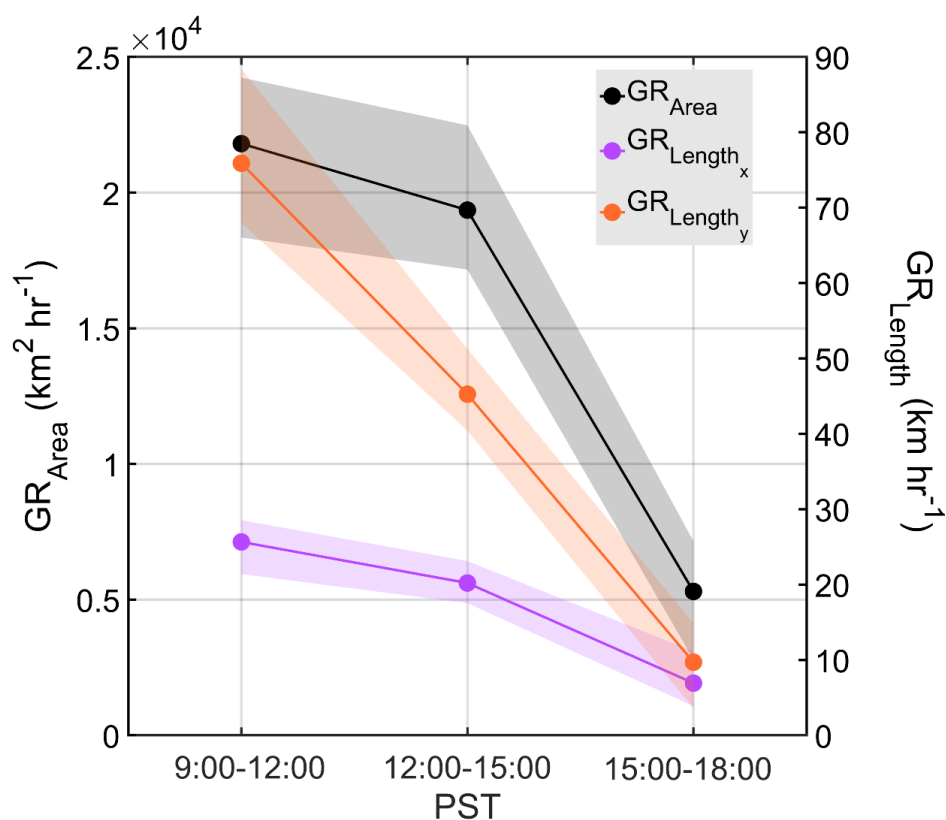


**Figure 4.** Diurnal profiles of (a) widest point of clearings at a fixed latitudinal value, (b) longest dimension between the maximum and minimum latitudinal coordinates of a clearing regardless of longitudinal value, (c) total clearing area, and (d) aspect ratio of clearing (i.e., width divided by length using the maximum values as described by panels a-b). The box and whisker plots show the median values (red points), the 25<sup>th</sup> and 75<sup>th</sup> percentile values (bottom and top of boxes, respectively), and minimum and maximum values (bottom and top whiskers, respectively).



1188



1189

1190

1191

1192

**Figure 5.** The median growth rate of clearing area (left y-axis) and width and length of clearings (right y-axis) over three hour increments. Shading of curves represents 95% confidence intervals calculated using bootstrapping ( $n=10,000$ ).



1193

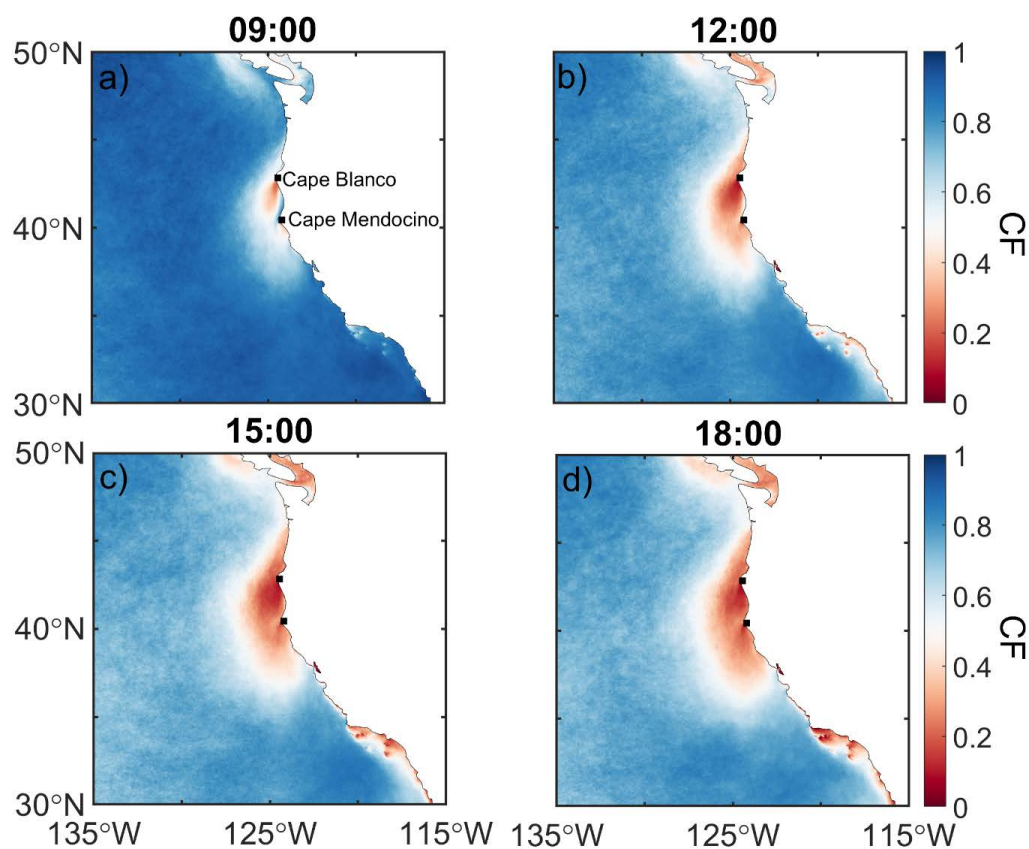


**Figure 6.** Diurnal profiles (PST times shown; add 7 h for UTC) of cloud fraction (CF) in the study region based on GOES imagery data from 306 clearing cases between 2009 and 2018 during JJA months.

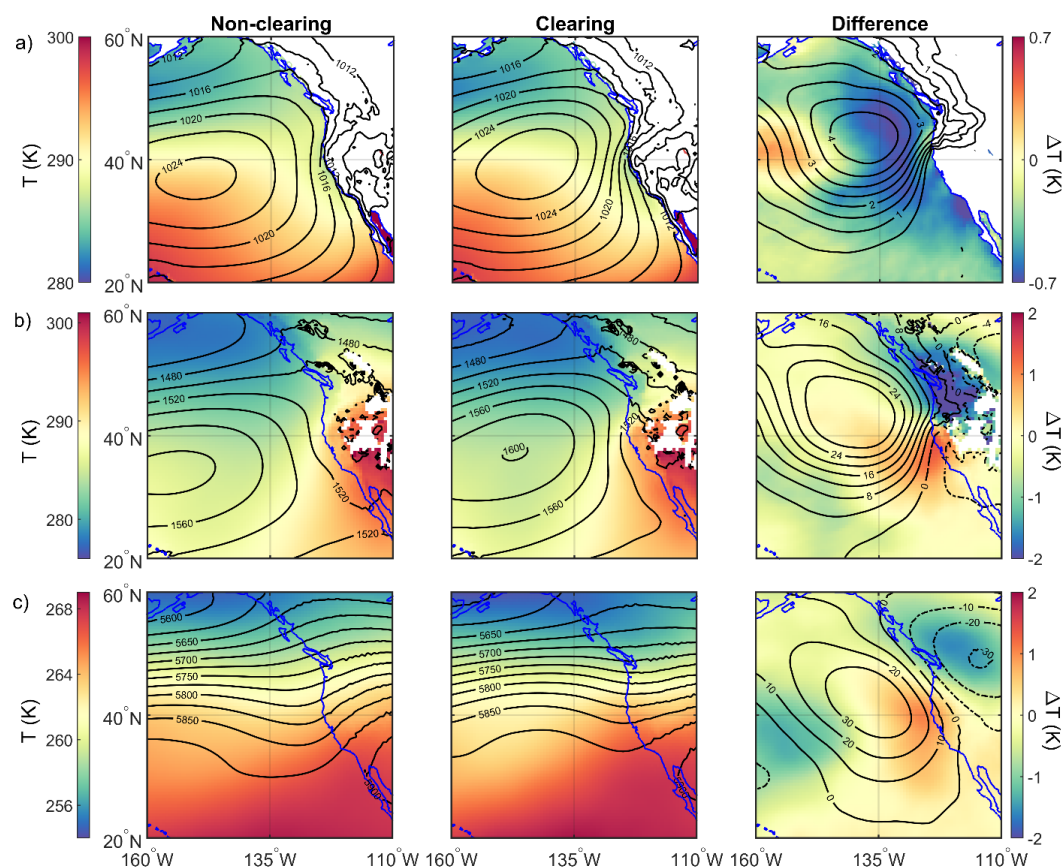


**Figure 7.** Climatology of non-clearing and clearing days as well as their differences (clearing minus non-clearing) during the summers (JJA) between 2009 and 2018 for a) mean sea level pressure (contours in hPa) and air temperature (color map) at sea surface, b) 850 hPa geopotential heights (contours in m) and air temperature (color map), and c) 500 hPa geopotential heights (contours in m) and air temperature (color map). The data were obtained from MERRA-2 reanalysis. Differences (clearing minus non-clearing) are shown in the farthest right column with separate color scales. White areas indicate no data were available.





1208

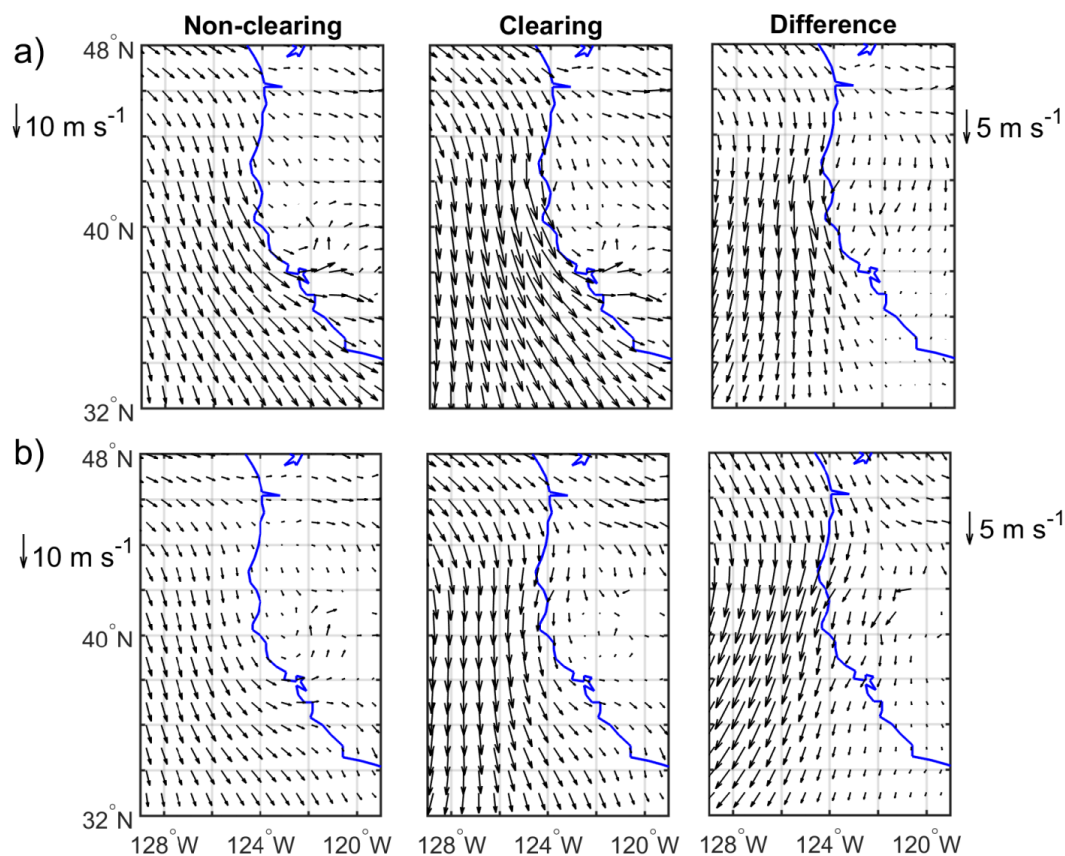


**Figure 8.** Same as Fig. 7 but for wind speed at the a) surface and b) 850 hPa. Reference wind vectors are shown for the left two columns, with separately define vectors for the difference (clearing minus non-clearing) plots on the far right.



1215

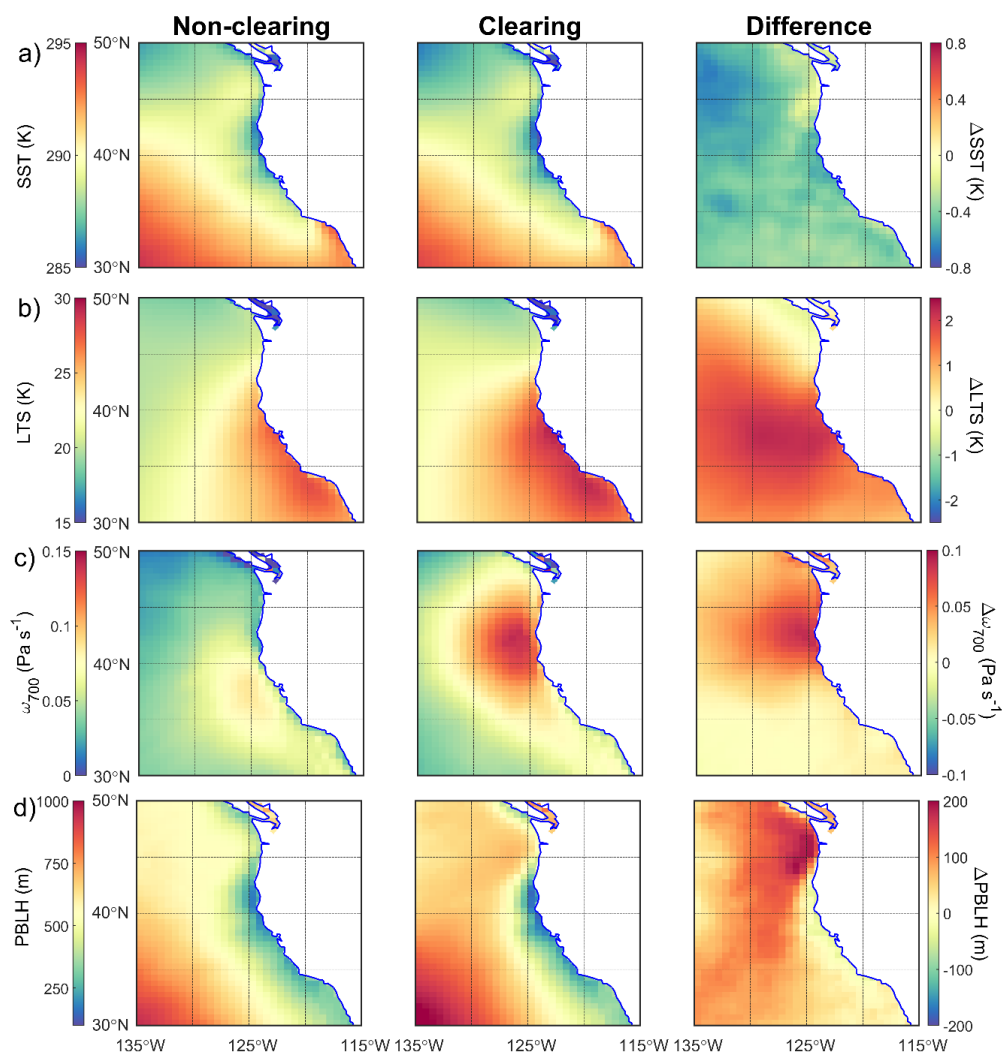
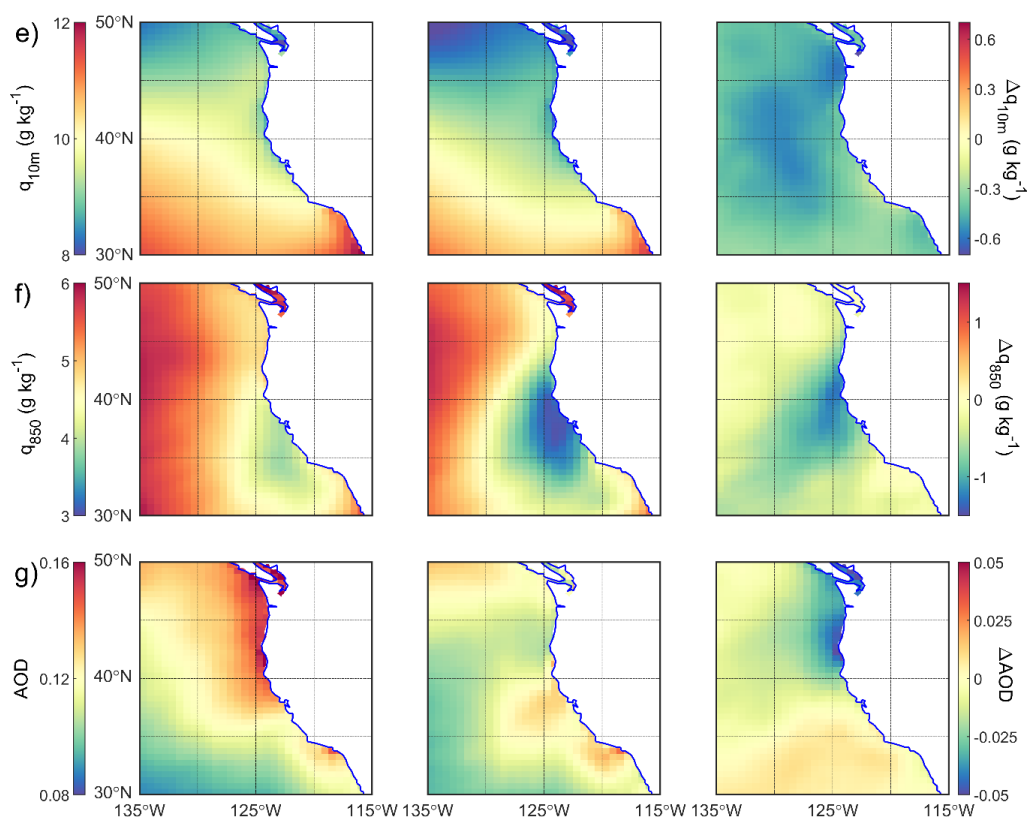


**Figure 9.** Spatial map of environmental parameters controlling properties of stratocumulus clouds for non-clearing and clearing events: a) sea surface temperature (SST), b) lower-tropospheric stability (LTS), c) vertical pressure velocity at 700 hPa ( $\omega_{700}$ ), d) planetary boundary layer height (PBLH), e) specific humidity at 10 m ( $q_{10m}$ ), f) specific humidity at 850 hPa ( $q_{850}$ ), and g) aerosol optical depth (AOD). Differences (clearing minus non-clearing) are shown in the farthest right column with separate color scales.



1225



1226

1227

1228 **Figure 9 (continued).**

1229

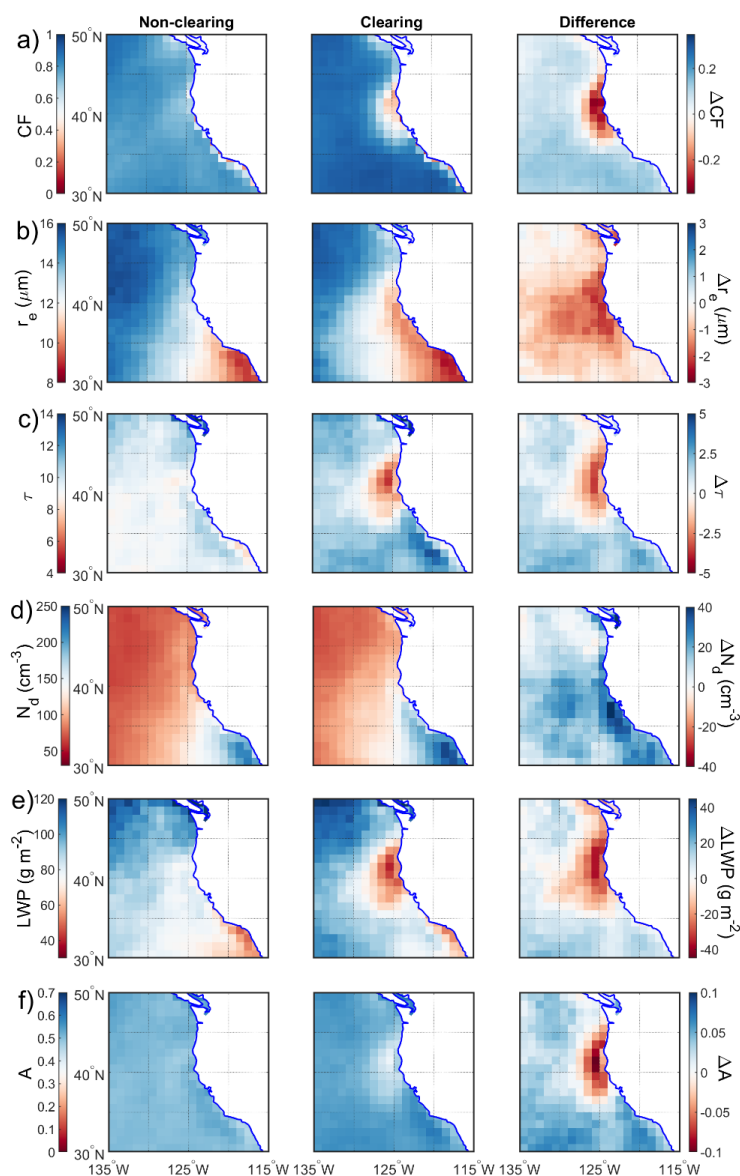


**Figure 10.** Average cloud parameters for non-clearing and clearing days obtained from MODIS Terra Level 3 (Collection 6.1) data: a) cloud fraction day (CF), b) cloud top droplet effective radius ( $r_e$ ), c) cloud optical thickness ( $\tau$ ), d) cloud droplet number concentration ( $N_d$ ), e) cloud liquid water path (LWP), and f) cloud albedo (A). Differences (clearing minus non-clearing) are shown in the farthest right column with separate color scales. Values from any instances of clear pixels were omitted from the analysis to produce panels b-f. Fig. S5 is an analogous figure based on MODIS Aqua data.

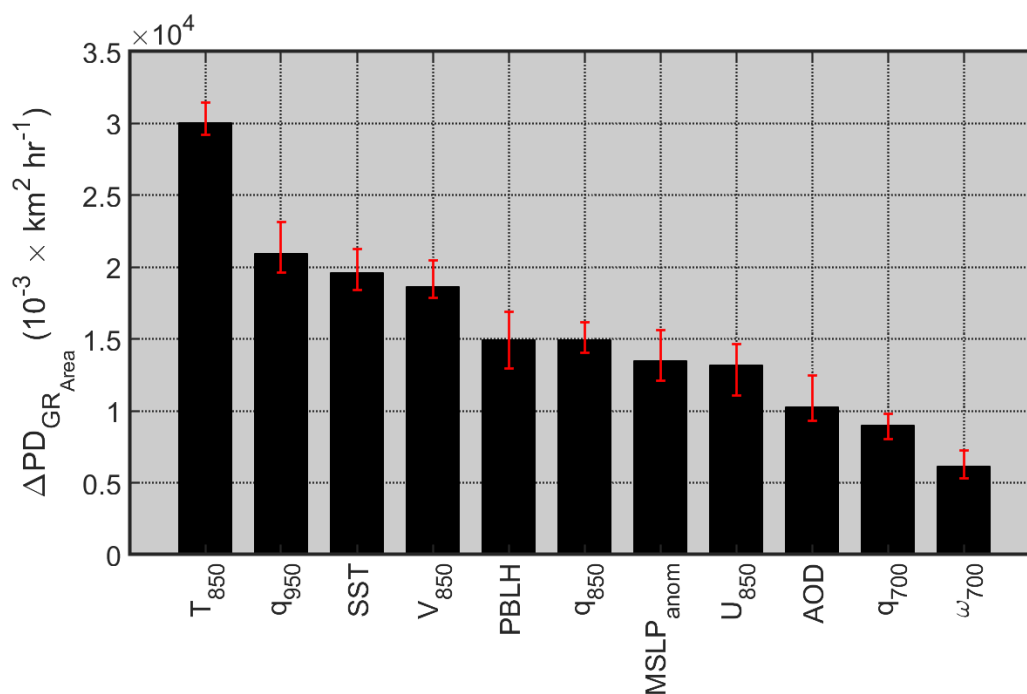


**Figure 11.** The median difference of maximum and minimum partial dependence (PD) of clearing growth rate ( $GR_{Area}$ ). Error bars represent the range of variability in 30 model runs. Note that GBRT simulations were performed using clearing growth rates obtained from the analysis of first and second GOES images (~09:00 – 12:00 PST) for all 306 clearing events examined.

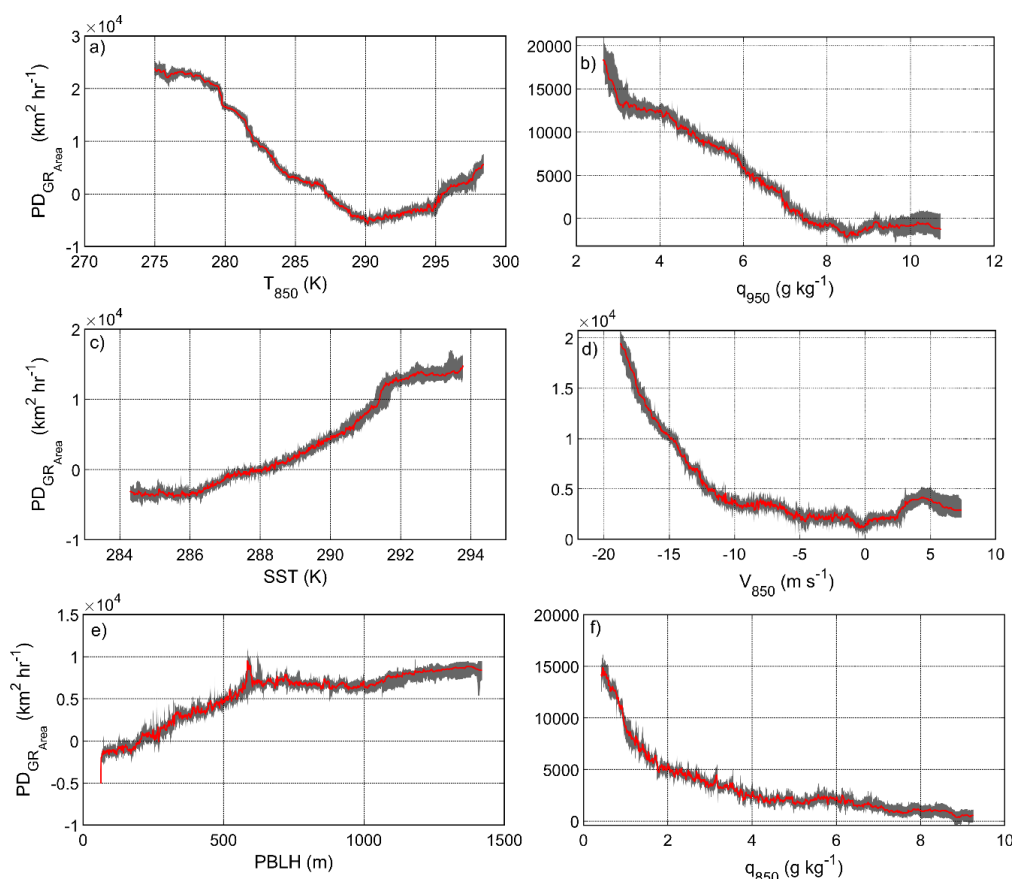


**Figure 12.** The median partial dependence (PD) of clearing growth rate ( $GR_{Area}$ ) on the following parameters: a) air temperature at 850 hPa ( $T_{850}$ ), b) air specific humidity at 950 hPa ( $q_{950}$ ), c) sea surface temperature (SST), d) meridional wind speed at 850 hPa ( $V_{850}$ ), e) planetary boundary layer height (PBLH), f) air specific humidity at 850 hPa ( $q_{850}$ ), g) mean sea level pressure anomaly ( $MSLP_{anom}$ ), h) zonal wind speed at 850 hPa ( $U_{850}$ ), i) aerosol optical depth (AOD), j) air specific humidity at 700 hPa ( $q_{700}$ ), and k) vertical pressure velocity at 700 hPa ( $\omega_{700}$ ). Red Shaded areas represent the range of variability of PD for 30 model runs. GBRT simulations were performed using clearing growth rates obtained from the analysis of first and second GOES images (09:00 – 12:00 PST) for all 306 clearing events examined.



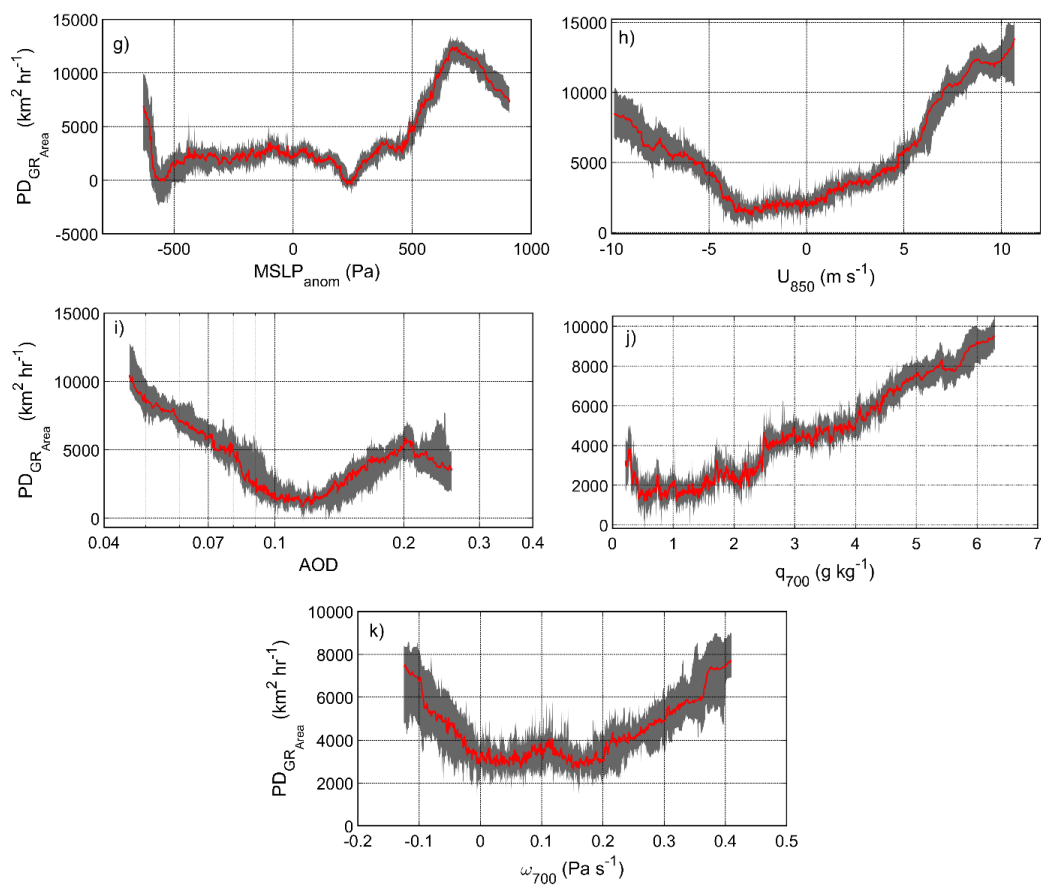


**Figure 12 (continued).**

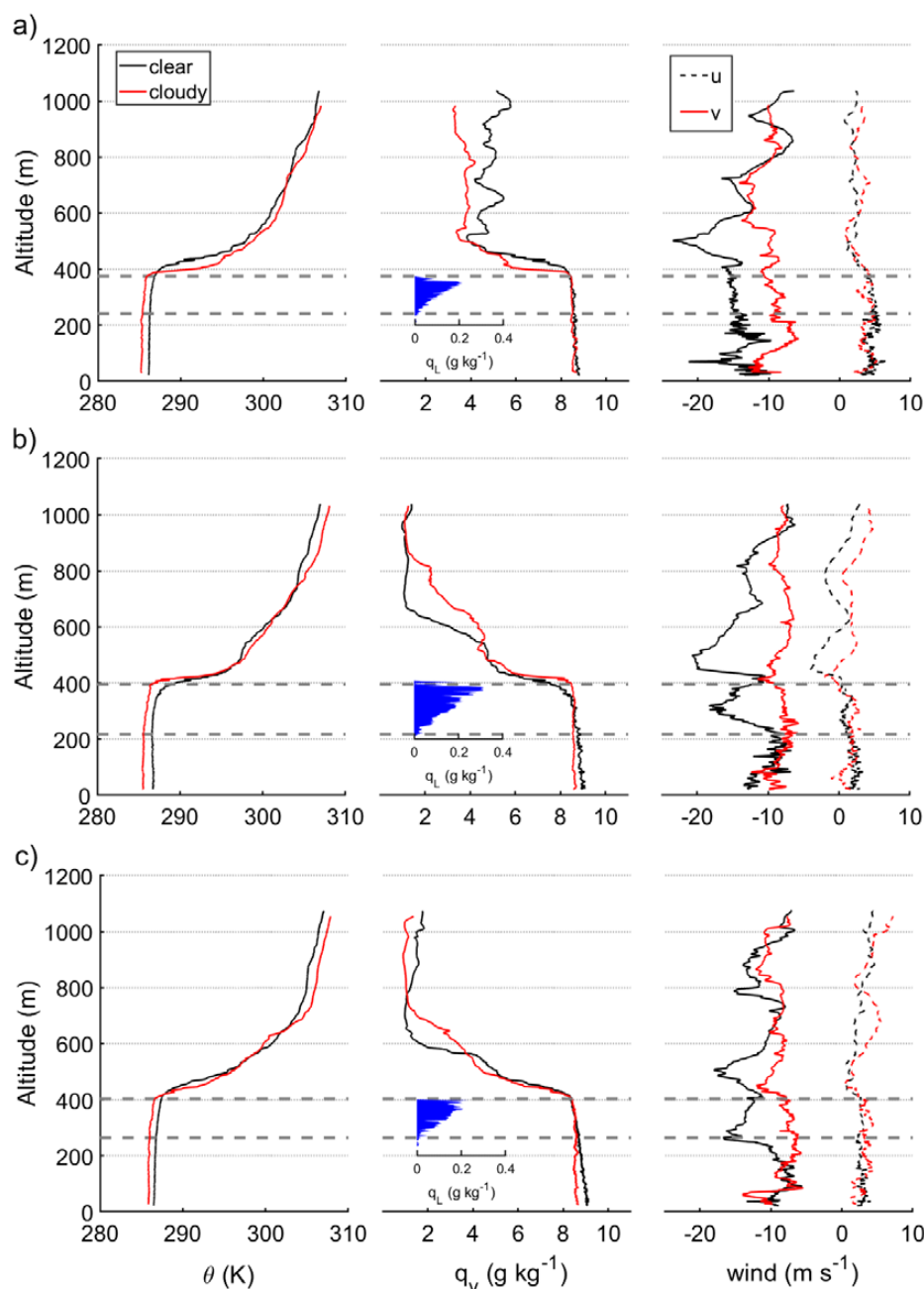


**Figure 13.** Sounding profiles of clear and cloudy columns for three case research flights examined in the FASE campaign: a) RF08, b) RF09A, c) RF09B. Horizontal wind speeds are decomposed into two components, ( $u$ ) perpendicular and ( $v$ ) parallel, relative to the cloud edge. Cloud borders are marked with dashed lines.

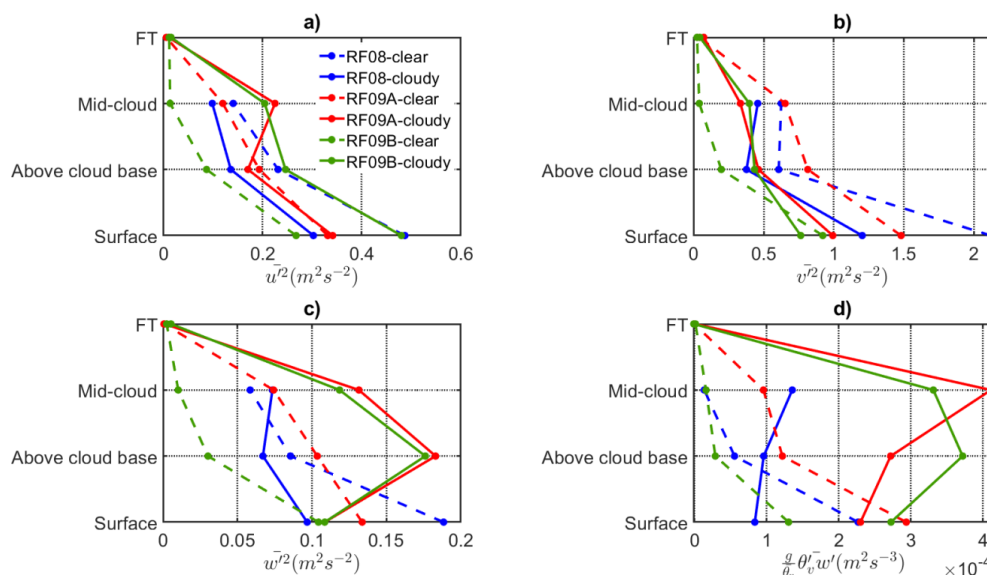


**Figure 14.** Selected dynamic parameters for the clear (dash lines) and cloudy (solid lines) parts of the legs performed at different altitudes for three FASE case research flights: Panels a-c) exhibit squared average velocity fluctuations of wind speeds components (u and v horizontal components, w vertical component). Horizontal wind speeds are decomposed into two components, (u) perpendicular and (v) parallel, relative to the cloud edge. Panel d) shows buoyancy flux profiles for the three flights.